Chemical and structural evolution of nano-oxides from mechanical alloying to consolidated ferritic oxide dispersion strengthened steel.

Gabriel Spartacus, Joël Malaplate, Frédéric de Geuser, Isabelle Mouton, Denis Sornin, Michel Perez, Raphaëlle Guillou, Benoit Arnal, Elodie Rouesne, Alexis Deschamps

Acta Materialia 233 (2022) 117992

Contents lists available at ScienceDirect

Acta Materialia

journal homepage: www.elsevier.com/locate/actamat

Chemical and structural evolution of nano-oxides from mechanical alloying to consolidated ferritic oxide dispersion strengthened steel

Gabriel Spartacus[a,b,*], Joël Malaplate[a], Frédéric De Geuser[c], Isabelle Mouton[a], Denis Sornin[a], Michel Perez[d], Raphaëlle Guillou[a], Benoit Arnal[a], Elodie Rouesne[a], Alexis Deschamps[c]

[a] CEA centre de Saclay, Université Paris-Saclay, CEA, Service de Recherches Métallurgiques Appliquées, Gif-sur-Yvette Cedex 91191, France
[b] (current affiliation) Department of Materials Science and Engineering, KTH Royal Institute of Technology, SE-100 44 Stockholm, Sweden
[c] Univ. Grenoble Alpes, CNRS, Grenoble INP, SIMAP, F-38000 Grenoble, France
[d] Univ. Lyon, INSA-Lyon, UCBL, MATEIS UMR CNRS 5510, F69621 Villeurbanne, France

ARTICLE INFO

Article history:
Received 16 November 2021
Revised 10 March 2022
Accepted 1 May 2022
Available online 4 May 2022

ABSTRACT

Ferritic Oxides Dispersion Strengthened (ODS) steels are of great interest for nuclear fission and fusion power plants. The nano-oxides embedded into the matrix provide the main contribution to the ODS steel strength. Understanding of the precipitation mechanism of ODS steels is thus critical for optimizing the fabrication process, involving Mechanical Alloying (MA) of Fe-14Cr, Y_2O_3 and TiH_2 powders. In this study, results from small-angle X-ray and neutron scattering, atom probe tomography and electron microscopy have been combined to investigate the nano-oxides evolution throughout the whole consolidation thermal treatment until 1100 °C. After MA clusters are observed, composed of Y, O and Ti. During heating these clusters grow and new ones nucleate, together with a sequential enrichment in Ti (from as-MA to 700 °C) and Y (between 900 and 1100 °C). A small quantity of Al is also found in the nano-oxides between 700 and 1100 °C. At 1100 °C the nano-oxides are found to be mainly $Y_2Ti_2O_7$ and subsequently progressively transform to Y_2TiO_5 during isothermal holding. Nano-oxides display however an unchanged extremely low coarsening rate, demonstrating the outstanding stability of both $Y_2Ti_2O_7$ and Y_2TiO_5 at 1100 °C.

1. Introduction

Ferritic Oxide Dispersion Strengthened (ODS) steels are one of the best candidates to be used as fuel cladding materials in Sodium-cooled Fast Reactors (SFR) of Generation IV nuclear power plants [1]. Moreover, ODS steels are also studied as potential structural materials of future nuclear fusion power plants [2]. Ferritic ODS steels for SFR applications are generally composed of a Fe-Cr-W matrix, containing a homogeneous dispersion of a high number density of nanometer-size Y-Ti-O precipitates. The body centered cubic (BCC) structure of the ferritic matrix exhibits high resistance to swelling under neutron irradiation [3,4], and its high Cr composition (>14 wt%) leads to good corrosion resistance, particularly important for the fuel reprocessing stage at the SFR fuel cladding end-of-life [4–6].

The nano-oxide particles act as strong pinning points for both dislocations and grain boundaries (GBs) until a temperature as high as 1200 – 1300 °C (around 70% of the melting temperature), due to their outstanding thermodynamic stability and sluggish coarsening at high temperature [7,8]. These properties lead to a great increase of thermal creep resistance [2,9-11] as well as yield strength [2,4,12]. Moreover, the nano-oxides – matrix interfaces efficiently trap He bubbles created from transmutations occurring under neutron irradiation, mitigating the irradiation-induced damage [13,14].

Nano-oxides are embedded in the matrix by means of powder metallurgy. During the process, a Fe-Cr atomized powder is milled together with a Y_2O_3 oxide powder by Mechanical Alloying (MA). Ti can be provided by an addition of a Ti-containing powder during MA (such as pure Ti or TiH_2) or as a pre-alloyed element of the Fe-Cr powder. During milling, the powder is subjected to se-

Abbreviations: ODS, Oxides Dispersion Strengthened; MA, Mechanical Alloying; SFR, Sodium-cooled Fast Reactors; GBs, Grain Boundaries; APT, Atom Probe Tomography; SAS, Small Angle Scattering; SAXS, Small Angle X-Ray Scattering; SANS, Small Angle Neutron Scattering; HE, Hot Extrusion; HIP, Hot Isostatic Pressing; TEM, Transmission Electron Microscopy; PCF, Pair Correlation Function; RDF, Radial Distribution Function.

* Corresponding author at: Brinellvägen 23, 11428 Stockholm, Sweden.
E-mail address: spartac@kth.se (G. Spartacus).

https://doi.org/10.1016/j.actamat.2022.117992
1359-6454/

vere plastic deformation, breakage and cold welding resulting in a high density of structural defects [15,16]. After optimization of the milling parameters, a homogeneous redistribution of Y, Ti and O among the ferritic matrix is generally found at the micrometer scale (no more Y- or Ti- rich large particles) [17–19]. The presence of amorphous particles is however sometimes observed [20], especially in model ODS alloys with a very high Y_2O_3 amount (10 to 25 wt%) [19,21,22]. Both Dai et al. (15 wt% Y_2O_3 addition) and Toualbi et al. (10 wt% Y_2O_3 addition) reported that the lattice parameter of the Fe-Cr matrix is only slightly higher after MA, and suggests that it should be due to Y_2O_3 oxides fragmentation up to very small particles, possibly amorphous, rather than a complete dissolution into the matrix [21,22].

At the nano-scale, several studies report the presence of inhomogeneity, whose distribution can only be resolved by Atom Probe Tomography (APT) or Small-Angle Scattering (SAS) measurements. In 2009, Kim et al. identified by Small Angle X-ray Scattering (SAXS) the presence of small particles in the as-MA powder of a Fe-9Cr ODS steel strengthened Y-Ti-O nano-oxides [23]. Oono et al. detected clustering of Y by APT measurements that seemed somewhat correlated to O on two Fe-15Cr ODS strengthened by Y-Ti-O and Y-O [24]. Alinger et al. identified small inhomogeneities by Small-Angle Neutron Scattering (SANS) at the as-MA stage thanks to the comparison of the scattering patterns of strengthened and non-strengthened powders [17]. Williams et al. reported the presence of clusters containing Y, Ti, O and Cr at the as-MA stage, visible by APT analysis on two Fe-14Cr ODS containing Ti and strengthened by an addition of Y_2O_3 or Fe_2Y [25,26]. Nevertheless, the matrix composition at the As-MA stage show that some Y, Ti and O are also dissolved in the Fe matrix [25].

Several ab-initio studies have been performed in order to investigate the stability of the constitutive elements of the nano-oxides (especially Y) into a ferritic matrix, as an attempt to explain the first stages of the nano-oxides formation. Among those studies, most agree on the possibility to form Y-vacancy and O-vacancy pairs in a BCC Fe matrix containing a high density of vacancies introduced by MA [27–32]. In particular, the Y-vacancy pair seems to greatly stabilize Y in the Fe matrix by lowering the compression field induced by the presence of Y at the interstitial position of the BCC lattice [29].

The O-vacancy pairs have attractive interaction with Y and Ti atoms [28,32]. Miller et al. found that the presence of Ti at interstitial position of the Fe lattice can also increase the stability of a neighbor O-vacancy pair [31]. Fu et al. found that the Y-O interaction is repulsive without vacancy [28], whereas Claisse et al. found it attractive (as well as the Ti-O interaction) [33]. In any case, the common attraction of Y(-vacancy) and Ti for O(-vacancy) could lead to their aggregation [28,33].

After MA, the powder is placed into a low carbon steel can, outgassed, and consolidated at a temperature around 1100 °C, generally by Hot Extrusion (HE) or Hot Isostatic Pressing (HIP). The nano-oxides precipitate during the increase of temperature, leading to a typical diameter of 2 to 3 nm and a high number density (10^{23} – 10^{24} m^{-3}) at the end of the process [8,17].

To date, there is still debate about the stoichiometry and structure of the nano-oxides after consolidation. The most commonly reported phase is the $Y_2Ti_2O_7$ pyrochlore, identified by Transmission Electron Microscopy (TEM) [8,34-38], by APT with chemical composition identification [39–41], by contrast-comparison of SAXS and SANS measurements [42], and by XRD analysis [23,24]. Hirata et al. also reported the $Y_2Ti_2O_7$ stoichiometry with a defective NaCl structure identified by TEM [43]. Several studies also identified Y_2TiO_5 orthorhombic nano-oxides by APT and TEM [36-38,44,45], as well as XRD identification [23]. Unifantowicz et al. also reported the identification of $YTiO_3$ orthorhombic structure by TEM crystallographic analysis [46]. Finally, Y_2O_3 has been reported, even in Ti containing ODS steels, with a BCC structure [24,35,37], and with a monoclinic structure [24]. These last precipitates are observed to be larger than the Y-Ti-O nano-oxides, and are known to exhibit faster coarsening [17,24,47]. The different possible phases of Y-O(-Ti) nano-oxides are summarized in Tab. 1.

Sakasegawa et al. proposed in 2009 a correlation between the size of nano-oxides and their nature, in a MA957 ODS steel (Fe-14Cr) [53]. The smallest precipitates (2 to 15 nm in diameter) were identified as non-stoichiometric Y-Ti-O, $Y_2Ti_2O_7$ stoichiometry was determined for 15 to 35 nm, whereas bigger ones correspond to Ti-oxides. Miller et al. reported similar results in a 14YWT alloy with $Y_2Ti_2O_7$ and Y_2TiO_5 identifications for 5 to 10 nm precipitates and non-stoichiometric Y-Ti-O for 1 to 4 nm precipitates [44]. Nevertheless, recent studies tend to demonstrate that very small nano-oxides of diameter 2 nm or even less, already have $Y_2Ti_2O_7$ or Y_2TiO_5 stoichiometry [36,45].

The chemical analysis of very small nano-oxides is generally performed by APT due to its ability to resolve the chemical elements at very small scale. It often reveals composition ratio of Y/Ti between ∼0.1 and ∼0.6 which is too low to correspond to any known phases [17,25,39,46,54]. However, APT suffers artefacts which could affect these ratios (ions trajectory overlaps, interface smearing, local magnification, atoms diffusion during evaporation…). Thus, even if artefact corrections have been proposed [41,79] the actual Y/Ti ratio of nano-oxides is still unclear, especially at early stages.

The experimental data on the evolution of the nano-oxides from the as-MA stage up to the annealing temperature of the nano-oxides are sparse due to the observation difficulties. The initial stage before heating, namely the as-MA material, is highly out-of-equilibrium, has a high density of crystal defects and is in powder form, which makes visualization of nanometer-size precipitates extremely challenging.

Oono et al. performed several 4 h isothermal heat treatments at different temperatures and observed the formation of $Y_2Ti_2O_7$ pyrochlore between 950 °C – 4 h and 1000 °C – 4 h [24]. Kim et al. performed 4 h isothermal heat treatments at different temperatures and several holding times at 1150 °C [23]. They observed the first formation of $Y_2Ti_2O_7$ with a pyrochlore structure between 800 °C – 4 h and 960 °C – 4 h. Then, during isothermal annealing at 1150 °C the Y_2TiO_5 orthorhombic structure was identified by XRD, starting from 4 h of holding, and displaying an increasing XRD peak intensity with holding time, suggesting an increase of volume fraction. However, their studied Fe-9Cr ODS steel exhibits a phase transformation of the matrix around 900 °C from BCC to face centered cubic (FCC), which could influence the nano-oxides precipitation mechanism [55,56]. Zhang et al. performed MA and subsequent thermal treatment directly on Ti and Y_2O_3 powders [57]. Their study shows the formation of $Y_2Ti_2O_7$ between 500 °C and 1000 °C with a maximum formation rate at 779 °C.

At the early stages of the thermal treatment, Alinger et al. observed an unreasonably high apparent volume fraction by SANS after 3h at 850 °C that decreased to more realistic levels after 3h at 1150 °C [17]. He et al. observed by SANS the same decrease of the apparent volume fraction of nano-oxides thanks to *in-situ* SANS measurements during isothermal holding at various temperatures [58]. Deschamps et al. performed SAXS *in-situ* measurements with a better time resolution during a heating ramp from as-MA to 800 °C and 900 °C followed by an isothermal annealing, more representative of the classical fabrication process [59]. The SAXS integrated intensity (from which apparent volume fraction can be calculated) of this study displayed an initial increase followed by a decrease before a stabilization after reaching the 900 °C plateau. The same behavior was more clearly identified in our previous paper, which allowed to monitor the precipitation kinetics of Fe-14Cr ODS nano-oxides up to 1100 °C *in-situ* with an excellent time res-

Table 1
Possible phases from the Y-O(-Ti) system taken into account in the present study.

Stoichiometry	Structure	Space Group	a (Å)	b (Å)	c (Å)	Ref.
$Y_2Ti_2O_7$	Pyrochlore	Fd-3m	10.089	10.089	10.089	[48]
Y_2TiO_5	Orthorhombic	Pnma	10.330	3.699	11.180	[49]
YTi_2O_6*	Orthorhombic	Pmnb	7.412	10.810	5.126	[50]
$YTiO_3$	Orthorhombic	Pbnm	5.690	7.613	5.338	[51]
Y_2O_3	BCC	Ia-3	10.596	10.596	10.596	[52]
Y_2O_3	Monoclinic	C12/m1	13.504	3.47	8.46	[52]

* Phase not experimentally identified in an ODS steel.

olution, but was not fully understood at the time [60]. The apparent volume fraction measured by SAXS or SANS is the product between the actual volume fraction and the contrast in scattering length density [61]. Therefore, the systematic decrease of the apparent volume fraction of SAS could indicate a significant change in chemical composition and/or structure of the nano-oxides during annealing, since their thermodynamic stability warrants that no dissolution should occur in this temperature range.

The present article aims at exploring the chemical and structural changes occurring during the ODS consolidation thermal treatment, from as-MA stage and up to 1100 °C and subsequent isothermal holding, using the complementarity of specific analytical techniques. In order to deconvolute the effects of chemistry, structure and volume fraction on small angle scattering signal, contrast variation methods will be carried out, namely combining on the same samples anomalous SAXS at the Y and Ti edges, which will allow to probe the presence of Y and Ti in the forming precipitates, as well as nuclear SANS. For the specific case of ASAXS at the Y edge, *in-situ* SAXS will additionally allow to follow the evolution of the presence of Y continuously during the heat treatment. These results will be supplemented by atom probe tomography, which will provide a reliable direct measurement of the number density of the nano-oxides and of the remaining solid solution in the matrix.

2. Materials and methods

2.1. Materials processing

In the present study, all ODS specimens were prepared by Mechanical Alloying (MA) of a Fe-14Cr-1W-0.3Mn-0.3Si-0.15Ni (in wt%) powder, with an addition of 0.3 wt% of Y_2O_3 and 0.3 wt% of TiO_2 powders by attrition milling. A milling duration of 10 h at the rotational speed of 440 rpm under high-purity argon atmosphere (99.9999%Ar) with a ratio of steel balls-over-powder of approximately 0.067 in weight (with steel balls being 440c steel) was applied. All milling was performed at the LTMEx laboratory of CEA research center. Subsequently to MA, the milled powders were densified by three different consolidation processes:

- Cold Pressing (CP), where the powder is placed in a commercial low-carbon steel cladding (ARMCO) and experienced a uniaxial pressure of around 3 GPa in order to achieve cylindrical specimens of ~ 4 mm in diameter. This process makes it possible to obtain ~80% densified specimen representative of the as-MA powder. These samples can then be heat treated during *in-situ* SAXS measurements or for ex-situ characterization at different stages of the heat treatment up to 1100 °C.
- Hot Extrusion (HE), where the powder is placed into a low carbon steel can and outgassed for 4 to 8 hours at a temperature ranging between 400 to 500 °C until a vacuum of 10^{-6} mbar is achieved. The can is then sealed and put into a furnace at 1100 °C, inducing a heating ramp of the powder at approximately 40 °C/min followed by an isothermal holding of ~1 h. Then, the can at 1100 °C is hot extruded under a load of 575 tons (for a can diameter of 75 mm) with a downstream motion of 25 mm/s with a section reduction around 12, and finally air-cooled at Room Temperature (RT). Afterwards, the material undergo an additional thermal treatment of 1 h at 1050 °C (subsequently air-cooled to RT) to release the internal stresses induced by HE.
- Hot Isostatic Pressing (HIP), where the steel can, after an outgassing process similar than that of the HE specimens, is put into a chamber with a rising temperature (at 4 °C/min) and pressure up to 1100 °C and 1.9×10^8 Pa followed by 2 hours of isothermal annealing and cooling at 4 °C/min.

For the elaboration of all the specimens, the same powder chemical composition and milling parameters were used. However, the powder for HE samples comes from a different milling batch than that of the CP and HIP samples.

At the end of the elaboration, a content ranging between 100 to 500 ppm of C, 100 to 700 ppm of N and 100 to 500 ppm of Al was systematically detected in the materials. The presence of these elements may result from impurities in the Fe-Cr atomized powder, from impurities introduced by the milling and from impurities introduced by the consolidation at 1100 °C (if applied) [62]. The measured chemical compositions are given for all alloys in Table 2.

2.2. Small Angle X-ray Scattering

Small Angle X-ray Scattering (SAXS) experiments were both performed *in-situ* during a thermal treatment and ex-situ on the CP material. The HE and HIP specimens were observed ex-situ after the consolidation process.

In-situ measurements were performed at the European Synchrotron Radiation Facility (ESRF) synchrotron at the D2AM-BM02 beamline. Samples of the CP material in the as-MA state were mechanically thinned to ~60 µm to achieve a suitable X-ray transmission at the used incident beam energy chosen just below the Y absorption K-edge (17.0384 keV). They were inserted in the custom-built *in-situ* furnace between two resistive heating parts drilled at the center to allow the X-rays to pass through. Temperature monitoring was ensured thanks to two thermocouples on both sides of the specimen, located as close as possible to the X-ray beam. The whole furnace was then put into a vacuum chamber. The detector to sample distance was set to 0.4 m and the SAXS scattering patterns were acquired on a 2D photon counting XPAD D5 hybrid pixel detector with a counting time of 10 sec. In order to analyze the anomalous effect linked to Y during the *in-situ* measurements, we used 2 incident energies, 16.829 keV and 17.009 keV corresponding to ~210 eV and ~30 eV below the Y absorption edge with an energy resolution of $\frac{\Delta E}{E} = 2 \times 10^{-4}$. The acquisition cycle included 5 image acquisitions followed by 1 transmission acquisition, at each energy, resulting in an energy switch every 60 s. The transmission was measured thanks to the acquisition of the scattering from a retractable kapton window which was removed for image acquisitions of the sample. Ex-situ measurements were also performed on several samples of CP, HE and HIP materials. These measurements were realized at 6 different energies: 16.829 keV,

Table 2
Measured chemical composition (in weight %) of the investigated specimens with the corresponding characterization techniques used.

Sample name	Cr	W	Ti	Y	O	C	N	Al
CP	13.9 [2]	1.13 [2]	0.27 [3]	0.16 [3]	0.15 [4]	0.031 [1]	0.032 [4]	0.030 [2]
HE	14.2 [2]	0.95 [2]	0.26 [3]	0.18 [3]	0.078 [4]	0.045 [1]	0.071 [4]	0.046 [2]
HIP	14.5 [2]	0.93 [2]	0.22 [3]	0.19 [3]	0.081 [4]	0.028 [1]	0.039 [4]	0.049 [2]

[1] combustion infrared absorption
[2] optical emission spectrometry
[3] plasma emission spectrometry
[4] reducing melting thermal conductivity

16.929 keV, 16.979 keV, 16.999 keV, 17.009 keV and 17.019 keV corresponding to ~210eV, ~110 eV, ~60 eV, ~40 eV, ~30 eV and ~20 eV below the Y K-edge respectively, in order to obtain a higher precision on the measurement of the anomalous effect.

Complementary anomalous SAXS measurements at the Ti K-edge (4.9664 keV) were performed at the Swiss Light Source (SLS) of the Paul Scherrer Institute (PSI) at the cSAXS beamline. For these experiments, the CP specimens followed interrupted or complete thermal treatment prior to the measurements and were measured ex-situ. Scattering patterns were acquired on two different 2D detectors, gathering the scattered X-ray at small (Pilatus 2M) and wide angles (off optical axis, Pilatus 300kw) with a detector to sample distance of respectively 2 m and 0.6 m. The measurement counting time was set to 10 sec and 15 frames were acquired and averaged at each of the 6 energies used: 4.766 keV, 4.866 keV, 4.916 keV, 4.936 keV, 4.946 keV, 4.956 keV corresponding to ~200 eV, ~100 eV, 50 eV, ~30 eV, ~20 eV, 10 eV below the Ti K-edge respectively with an energy resolution of $\frac{\Delta E}{E} < 2 \times 10^{-4}$. Due to experimental difficulties, some samples were only measured at 5 energies. The sample thickness was set to ~20 µm by mechanical grinding or electrochemical polishing.

Laboratory SAXS measurements were performed using a Mo rotating anode X-ray source (19.447 keV). SAXS patterns were acquired on a Pilatus2 300k 2D detector with a specimen to detector distance of ~0.8 m. Measurements counting time was 200 s for each of the 5 averaged frames used per measurement.

For every SAXS measurement, the 2D scattering data was azimuthally integrated, background subtracted, and normalized for solid angle, specimen thickness, transmission and incident beam flux. SAXS intensity was then reduced to absolute unit thanks to a glassy carbon secondary standard. SAXS experimental measurements were then fitted to a simulated model of a lognormal distribution of spheres with a dispersion fixed to 20% [63]. This model can be expressed as followed:

$$I(q) = A.q^{-n} + I_{ppt}(q) + K \tag{1}$$

The first term represents the background scattering at small scattering vectors. This contribution arises from the combination of Porod scattering of coarse precipitates (carbides, nitrides ...) or porosities inducing a signal proportional to q^{-4}, and from a high density of dislocation, inducing a signal proportional to q^{-3}. As the thermal treatment evolves, starting from the highly deformed as-MA initial stage, the intensity of these two contributions is expected to vary significantly. Therefore, a $A.q^{-n}$ contribution with n ranging between 3 and 4 was chosen. The model also considers a constant contribution (K), predominant at high q values, which results from the Laue scattering of the disordered solid solution and from other sources of incoherent scattering (*e.g.* fluorescence).

$I_{ppt}(q)$ is the intensity arising from a lognormal distribution of spherical precipitates (with a small volume fraction $f_v \ll 1$) which can be expressed as:

$$I_{ppt}(q) = \int_{r=0}^{+\infty} f(r)\ \Delta\rho_{e^-}^2 \left(\frac{4}{3}\pi r^3\right)^2 F(r,\ q)^2\ dr \tag{2}$$

With $f(r)$ the density of probability of a lognormal distribution of sphere with a mean radius R_m and a dispersion of 20%, $\Delta\rho_{e^-}$ the electronic contrast between the matrix and the precipitates and $F(r,\ q)$ the Rayleigh form factor of a sphere.

In summary, 5 parameters of the model were fitted to match with the experimental data:

- R_m the mean radius of the precipitates.
- $\Delta\rho_{e^-}^2 \times f_v$ the square of the electronic contrast times the volume fraction of the precipitates
- A the intensity of the Porod contribution.
- n the power of the Porod contribution, varying between 3 and 4
- K the constant Laue scattering.

Anomalous SAXS measurements aims at probing the presence of an element in the precipitates and / or in the matrix. They consist in performing measurements at different incident energies nearby the absorption edge of the element to probe. At least two energies must be probed, one far and one close to the absorption edge. If the concentration of the probed element is different in the precipitates and in the matrix, the intensity of the precipitate contribution of the scattered intensity (*i.e.* $I_{ppt}(q)$) will be energy-dependent. In the present case, two elements were probed: Y and Ti. These elements are in low concentration in the matrix with a nominal composition of 0.24 wt% for Y and 0.29 wt% for Ti. Thus, in the following we will neglect the variation of the matrix compositions and only consider the composition of Y and Ti in the precipitates.

To discriminate between the different possible phases, we have used the method developed by Dumont *et al., i.e.* calculated the experimental "anomalous factor" named ϕ^Y and ϕ^{Ti} for the measurements performed at the Y K-edge and at the Ti K-edge respectively [64]. As demonstrated in details by Dumont et al. the square root of $\Delta\rho_{e^-}^2 \times f_v$ (retrieved by model fitting) obeys by a linear relationship to the scattering factor of the probed element, noted $f_k(E)$ for the element k (Y or Ti), and taken with an incidence angle of zero in the case of SAXS measurements [64].

$$\sqrt{\Delta\rho_{e^-}^2(E) \times f_v} = \sqrt{f_v}\left(\sum_{i\neq k}\left(\frac{X_{i,ppt}}{V_{at,ppt}} - \frac{X_{i,m}}{V_{at,m}}\right) f_i + \left(\frac{X_{k,ppt}}{V_{at,ppt}} - \frac{X_{k,m}}{V_{at,m}}\right) f_k(E)\right) \tag{3}$$

Here, i represent all the elements (apart from the element k) present in the alloy with an absorption edge far away from E. $V_{at,ppt}$ and $X_{i,ppt}$ are the mean atomic volume and the atom fraction of atom i in the precipitates, and similarly for $V_{at,m}$ and $X_{i,m}$ in the matrix. These two values can be retrieved from the linear regression of $\sqrt{\Delta\rho_{e^-}^2(E) \times f_v}$ in function of $f_k(\lambda)$, allowing to calculate the experimental anomalous factor, defined as:

$$\phi^k = \frac{\sum_{i\neq k}\left(\frac{X_{i,ppt}}{V_{at,ppt}} - \frac{X_{i,m}}{V_{at,m}}\right) f_i}{\left(\frac{X_{k,ppt}}{V_{at,ppt}} - \frac{X_{k,m}}{V_{at,m}}\right)} \tag{4}$$

This experimental anomalous factor can then be compared to theoretical values calculated from the composition and atomic volume of the matrix and the different precipitates phases given in Tab. 1. An error bar has been estimated for the theoretical anomalous factors to take into account the cell parameters uncertainties and their evolution with the temperature (for the matrix and the precipitates) during *in-situ* measurements.

As the determination of the experimental factors are based on linear regression, increasing the number of measured energies increases its precision. Ex-situ samples have therefore been measured at 6 energies. For the ex-situ measurements, the R^2 value of the linear regression was always higher than 0.95, and mostly higher than 0.98. *In-situ* measurements were performed at only 2 energies to keep a satisfactory time resolution, with a cost in uncertainty which is partly mitigated by the fact that we have a continuous estimation of the anomalous factor. To compare the intensity at the two levels of energy for the same ageing time, an n-spline interpolation has been performed.

2.3. Small Angle Neutron Scattering

SANS measurements have been performed on the PAXY beamline of the ORPHEE nuclear reactor at the CEA Saclay. Measurements were performed on CP specimens that followed several interrupted thermal treatments (also measured by SAXS). Scattering patterns were acquired on a 2D detector with a specimen to detector distance of ~2 m and at a wavelength of 6 Å. The sample thickness was measured prior to the experiment and was for all samples around 1 mm. For the experiments, the measured specimens were subjected to a strong magnetic field (~1.6 T) in the horizontal direction. This field allowed to deconvolute the magnetic I_{mag} and nuclear I_{nuc} intensities by a least square fitting of the $I_{mag} + \sin^2(\alpha) I_{nuc}$ dependence, with α the angle from the applied magnetic field, as shown in previous SANS studies on ODS steels [17,65,66]. I_{mag} and I_{nuc} respectively arises from the magnetic and nuclear contrast between the matrix and the precipitates. In ODS steels the Y-Ti-O nano-oxides are generally considered as magnetic hole [17,65]. In the present study, probably because of the presence of non-stabilized clusters in low annealing conditions and because of the extremely small size of the nano-oxides in more advanced annealing conditions, the magnetic hole hypothesis has been considered as not reliable enough for chemical and structural examination of the nano-oxides. Therefore only the nuclear contribution was taken into account, likewise with the work of Ohnuma et al. who compared the SAXS and SANS nuclear contrast to extract information of the nano-oxides nature in a fully consolidated ODS steel [42].

Similarly to SAXS experiments, SANS scattering pattern were background subtracted and normalized by solid angle, sample thickness and transmission as well as incident beam intensity. The intensity was reduced to absolute unit thanks to the scattering of a Plexiglas secondary standard. The experimental data (I_{nuc}) were then fitted using the following model:

$$I_{nuc}(q) = A.q^{-n} + I_{ppt}(q) + K_{inc} \tag{5}$$

With K_{inc} a constant arising mainly from the incoherent scattering of the matrix and $I_{ppt}(q)$ the intensity coming from the precipitates, and can be expressed similarly to the Eq. 6 by replacing the electronic contrast $\Delta\rho^2_{e^-}$ by the neutron nuclear contrast $\Delta\rho^2_{nuc}$ between the matrix and the precipitates. The values of this nuclear contrast are calculated from the values of scattering length of each elements available in the ILL Neutron Data Booklet [67].

2.4. Transmission and Scanning Electron Microscopy

Nano-oxides size measurements were performed from TEM images analysis acquired on a JEOL 3010 operating at 300 kV thanks to ImageJ/Fiji Weka Trainable Segmentation algorithm [68] and post-treatment using Matlab. TEM orientation mapping and Energy Dispersive Spectrometry (EDS) images were performed on a JEOL 2100F microscope operating at 200 kV in Scanning mode (STEM). For all the TEM observations, samples were electro-polished thanks to a solution of 10% perchloric acid and 90% of ethanol at -10 °C thanks to a Struers Tenupol thinning device.

2.5. Atom Probe Tomography

Specimens were prepared by a FEI Dual Beam Hélios nanolab 650 Focused Ion Beam (FIB) using a lift-out technique at the as-MA stage (2 samples probed) and after interrupted thermal treatments at various temperatures (1 sample per thermal treatment). Extracted specimens were then needle-shaped by FIB to be suitable for APT experiment. APT measurements have been performed on a LEAP 4000X HR instrument equipped with a reflectron in laser mode. The specimen's temperature was set to 60 K with laser energy of 60 pJ and a frequency varying between 125 kHz and 200 kHz depending on the continuous electric field evolution. 3D reconstructions were performed with IVAS 3.6.14 commercial software.

The DIAM algorithm (distribution of isolated atoms for the determination of the matrix composition) was used to extract the matrix composition of each APT volume following the method described by De Geuser and Lefebvre [69]. For this analysis, the first nearest neighbor distances (1NN) were calculated using IVAS software and further calculations were performed using Matlab. To ensure that the region surrounding grain boundaries do not influence the results, these were removed from each of the APT volumes. The DIAM method aims at extracting the composition of the matrix (without precipitates) from an APT reconstruction through the calculation of the probability to find an isolated atom (P_{iso}) in a virtual sphere of radius r. For a dilute element in solid solution this probability follows a Poisson law and $P_{iso}(r) = e^{-n}$ with $n = -\frac{4}{3}\pi r^3 \times \rho_0$ the average number of atoms in a sphere of radius r, with a bulk atom density ρ_0. If the APT volume contains precipitates, this probability will be modified as such:

$$P_{iso}(r) = x\, e^{-\rho_{ppt}/\rho_0 n} + (1-x)\, e^{-\rho_m/\rho_0 n} \tag{6}$$

With ρ_{ppt} and ρ_m the atom density of the precipitates and the matrix respectively and x the fraction of atoms that belongs to the precipitates. A linear regression of $\ln(P_{iso}(r))$ at high n values – where the matrix contribution is predominant – can then allow to retrieve ρ_m.

The number density of clusters was extracted by the maximum separation method using the IVAS software. For this method, the maximum separation distance (d_{max}) was set for each volume based on the experimental and randomized 1NN of (Y, YO), in order to identify a maximum of clusters and minimize the false positive cluster identification, following the method described by Dhara et al. [70]. The minimum amount of atoms to define a cluster (N_{min}) was set at different values ranging from 6 to 12 to calculate error bars (standard deviation).

Pair Correlation Functions (PCF) were calculated from the Radial Distribution Function (RDF) generated by IVAS, similarly to Zhao et al. [71], and are expressed for a central atom i and neighbor atom j in a virtual sphere of radius r as:

$$\gamma_{i-j}(r) = f_v(1-f_v)\left(C^i_{ppt} - C^i_m\right)\left(C^j_{ppt} - C^j_m\right)\gamma^0(r) \tag{7}$$

Where C^i_{ppt} and C^i_m are the precipitates and matrix concentration of the atom i respectively, and $\gamma^0(r)$ the normalized PCF only re-

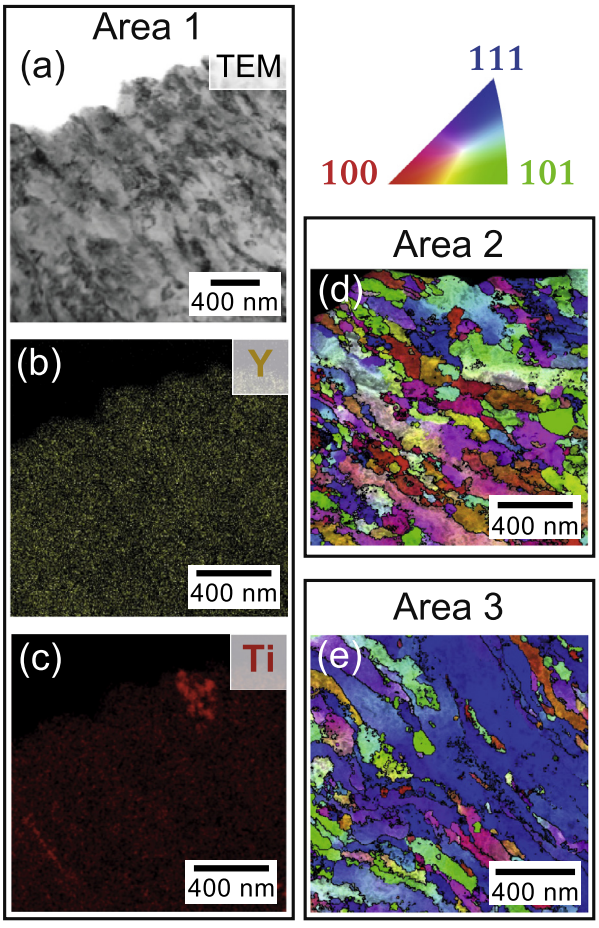

Fig. 1. TEM image in bright field (a), with the corresponding TEM/EDS images showing the Y (b), and Ti elemental maps (c) displaying homogeneous distribution of Y and a local Ti enrichment, along with ASTAR orientation mapping showing a highly deformed matrix (d, e) in two different areas of the CP-14Cr specimen.

lated to the size distribution of the spherical precipitates. The autocorrelation functions $\gamma_{i-i}(r)$ were then fitted to the experimental data, using the same dispersion of the lognormal distribution than SAS fitting ($s = 0.2$) in order to retrieve for each elements a mean radius of precipitates as seen by APT and $f_v(1-f_v)(C^i_{ppt} - C^i_m)^2$ the chemical contrast between the matrix and the precipitates correlated to the volume fraction of precipitates. This approach allows a straightforward comparison of SAS and APT data, as their result are extracted from the same model, under the same assumptions (lognormal distribution of spheres), transposed into the direct space.

3. Results

This section is divided in two parts focusing first on the characterization of the microstructure of the initial as-MA stage and secondly on the nano-oxides chemical composition and structural evolution.

3.1. Microstructure characterization of the as-MA stage

Observations performed by TEM using EDS mapping and ASTAR orientation are shown in Fig. 1. These results display an extremely deformed microstructure with nano-sized grains clearly visible in bright field and in orientation mapping (Fig. 1a, Fig. 1d and Fig. 1e). The shape of the nano-grains varies from one area to another, from equiaxed (Fig. 1d) to elongated (Fig. 1e). This shape inhomogeneity is probably linked to variation of local deformation occurring during MA or subsequent cold pressing. The granular microstructure is similar to the observation of Sallez et al. on a grain extracted from an as-MA powder [72]. The EDS mapping at high magnification reveals small local enrichment in Ti (Fig. 1c). Due to its very small size and the highly deformed matrix, it is difficult to determine whether this Ti enrichment is linked to the presence of a Ti-rich precipitates (such as Ti oxides or carbonitrides). No inhomogeneities could be identified at this scale on the Y elemental map (Fig. 1b).

3.2. Chemical and structural evolution of the nano-oxides

The chemical evolution of the nano-oxides has been investigated using several characterization methods, involving X-ray and neutron as well as atom probe tomography. These results will be presented in 3 different subsections for clarity and will be then carefully compared and correlated in the discussion part.

3.3. Small angle X-ray scattering

Our previous article focused on the description of the precipitation kinetics (evolution of mean radius comparing two heating rates) using *in-situ* SAXS is available in reference [60], the present section will therefore only focus on the chemical evolution of the nano-oxides, especially using the anomalous scattering analysis (previously not reported). The SAXS intensity curves for the *in-situ* heat treatment and for interrupted thermal treatments can be founded in ref. [60]. The results in terms of mean radius (R_m) and $\Delta\rho^2_{e^-} \times f_v$ of the nano-oxides are displayed in Fig. 2a and Fig. 2b respectively, for the heating rate of 10 °C/min representative of the HIP process. On this plot, the heating ramp is described with a temperature scale and the subsequent isothermal holding at 1100 °C with a time scale. This representation favors the comparison of this dataset with the one recorded at 30 °C/min, representative of the HE process, displayed in Fig. 3a and Fig. 3b. The ex-situ measurements represented as stars (for R_m) or triangles (for $\Delta\rho^2_{e^-} \times f_v$) were measured either before/after the *in-situ* heat treatment or after an interrupted thermal treatment.

As previously reported [60], a scattering signal is detected in all specimens at the as-MA stage. It corresponds to the presence of chemical fluctuations that can be assimilated to very small clusters as seen in Fig. 2a and Fig. 3a. These initial clusters start to grow around 450 °C and show a remarkable thermal stability at 1100 °C, with a mean radius of ~1.3 nm (irrespectively of the heating rate).

On Fig. 2b and Fig. 3b, a difference can be noticed between the $\Delta\rho^2_{e^-} \times f_v$ taken at the energy E_1 and at the energy E_2. This gap, present from the as-MA stage (also visible on the ex-situ measurements) and all along the thermal treatment, indicates the presence of Y inside the clusters / precipitates. Moreover, $\Delta\rho^2_{e^-} \times f_v$ at the energy E_2 (close to the Y K-edge) is systematically higher as compare to the energy E_1 (far from the Y K-edge). As the electronic density of Y-rich precipitates drop when the energy come closer to the Y K-edge, an increase of the electronic contrast (difference between the electronic density of the precipitates and the matrix in absolute value) implies a lower electronic density of the precipitates as compared to the surrounding matrix (Fe-14Cr BCC), all along the heat treatment.

The overall evolutions of the curves shown in Fig. 2b and Fig. 3b is similar with an initial rise of the signal around 450 °C (concomitant with the R_m increase) and a subsequent decrease of the signal after 800 to 900 °C. The first increase of $\Delta\rho^2_{e^-} \times f_v$ signal is likely linked to an increase of the volume fraction of nano-oxides due to the growth of the existing clusters and / or the nucleation of new ones. The decrease in $\Delta\rho^2_{e^-} \times f_v$ however, cannot be due to a decrease of the volume fraction, as the nano-oxides should not dissolve at this temperature. Therefore, this decrease is more

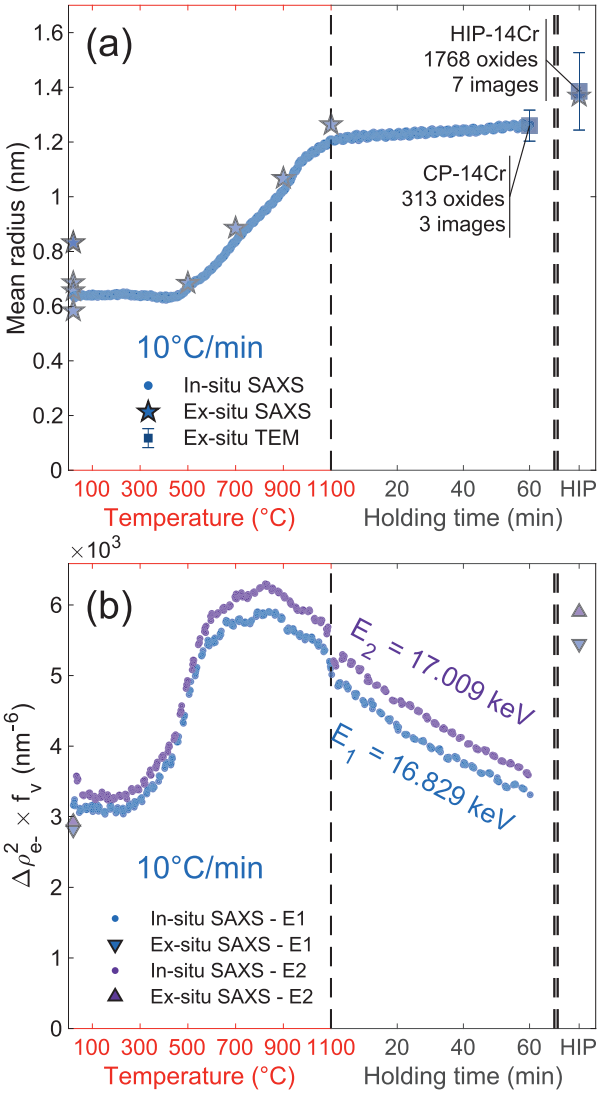

Fig. 2. Evolution of the mean radius (a), and $\Delta\rho_{e^-}^2 \times f_v$ (b), of the nano-oxides upon a 10 °C/min heating rate on the CP-14Cr and HIP-14Cr specimens extracted from SAXS data.

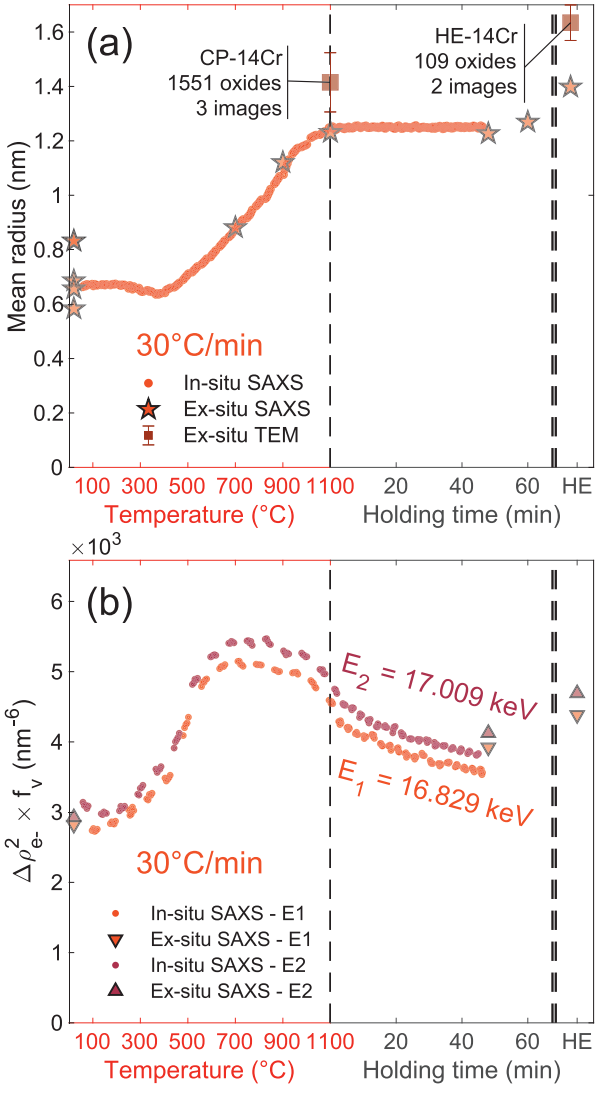

Fig. 3. Evolution of the mean radius (a), and $\Delta\rho_{e^-}^2 \times f_v$ (b), of the nano-oxides upon a 30 °C/min heating rate on the CP-14Cr and HE-14Cr specimens extracted from SAXS data.

likely linked to a change in the electronic contrast and therefore to a change of chemistry and / or structure of the nano-oxides during heating. The mean radius of precipitates in the CP material at the end of the thermal treatment (10 and 30 °C/min) are similar to that of the HIP and HE materials. The $\Delta\rho_{e^-}^2 \times f_v$ of the CP material after 30 °C/min heating is close to the value on the HE sample, however, the $\Delta\rho_{e^-}^2 \times f_v$ of the CP material after 10 °C/min heating appears lower than the HIP sample.

Fig. 4 displays the SAXS scattering intensity curves acquired at the Ti K-edge on several specimens that followed an interrupted or complete thermal treatment with a heating rate of 30 °C/min. For visibility purpose, the curves on the CP specimens (Fig. 4a) at several temperatures were artificially shifted by a decade. The least-square fitted curves are plotted as continuous lines.

The mean radius and $\Delta\rho_{e^-}^2 \times f_v$ extracted from these SAXS patterns are displayed in Fig. 5a and Fig. 5b along with *in-situ* data from the experiments at the Y K-edge. A slight shift of around 0.1 nm is observed between the measurements made at the ESRF and those made at the PSI synchrotron (Fig. 5a), even if mean radii extracted from different SAXS experimental setup are generally known to have a good consistency [73]. This shift is probably due to the influence of the texture of coarse precipitates causing some signal anisotropy, which is visible on the PSI SAXS intensity curves and not on the ESRF and laboratory SAXS intensity curves, possibly because of experimental setup differences. Therefore, the results given by ESRF and laboratory facilities should be considered more accurate in terms of nano-oxides mean radius. Nevertheless, this R_m shift should not affect the quality of the anomalous SAXS analysis at the Ti K-edge, which represents the most valuable data. Once again, the mean radius of nano-oxides is found very consistent between CP and HE specimens.

Unfortunately, no measurement could be achieved from the as-MA stage until 700 °C annealing due to the difficulty to prepare a good quality 20 µm thick specimens from non-annealed CP samples. Nevertheless, the difference between the $\Delta\rho_{e^-}^2 \times f_v$ taken at different energies could be detected from the 700 °C stage and until 1100 °C – 1 h (Fig. 5b). The anomalous effect evidences the presence of Ti inside the precipitates from the lowest temperatures probed (700 °C) until the end of the thermal treatment. The global evolution of the $\Delta\rho_{e^-}^2 \times f_v$ curves at the Ti K-edge is consistent with the $\Delta\rho_{e^-}^2 \times f_v$ evolution at the Y K-edge (Fig. 2b and Fig. 3b), showing first an increase and then a decrease of the signal, followed by a moderate evolution.

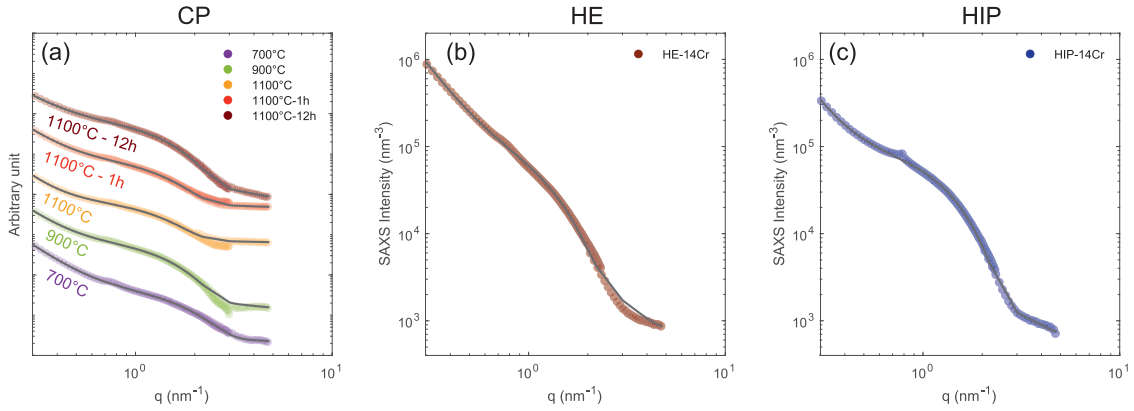

Fig. 4. SAXS scattering intensity curves on CP-14Cr specimens, showing the evolution of the precipitate contribution toward lower q-values (*i.e.* bigger precipitates) (a), HE-14Cr specimen (b) and HIP-14Cr specimen (c), displayed at 4.766 keV along with the fitted model in continuous line.

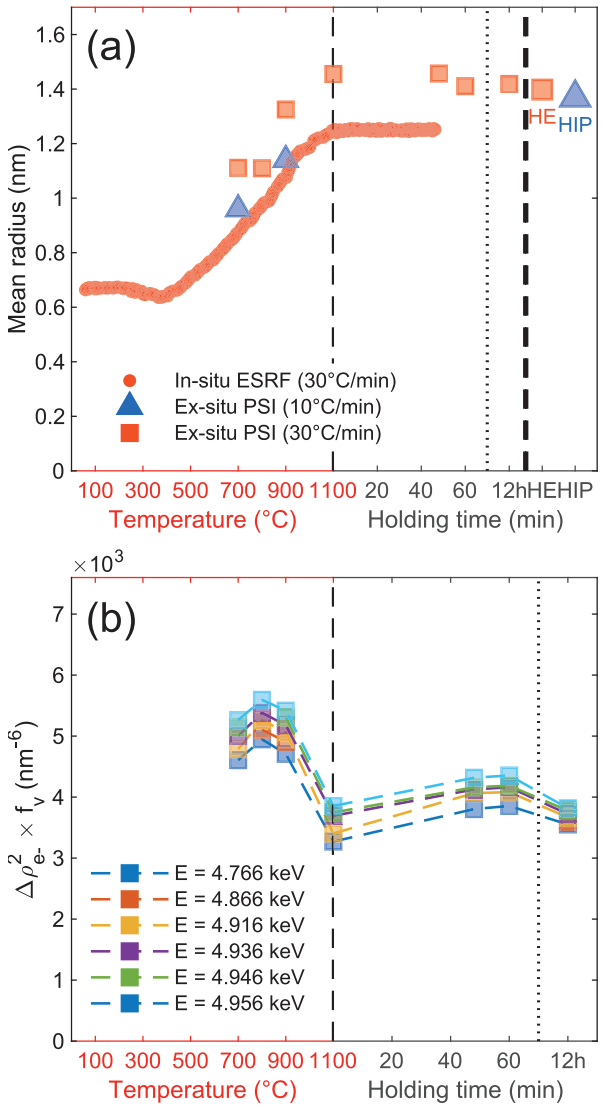

Fig. 5. Mean radius evolution at different stages of the interrupted thermal treatment measured at PSI synchrotron and compared with *in-situ* measurements acquired at the ESRF synchrotron (a), and evolution of the $\Delta\rho_{e^-}^2 \times f_v$ of the nano-oxides SAXS contributions at several energies close to the Ti K-edge (b), on CP-14Cr specimens.

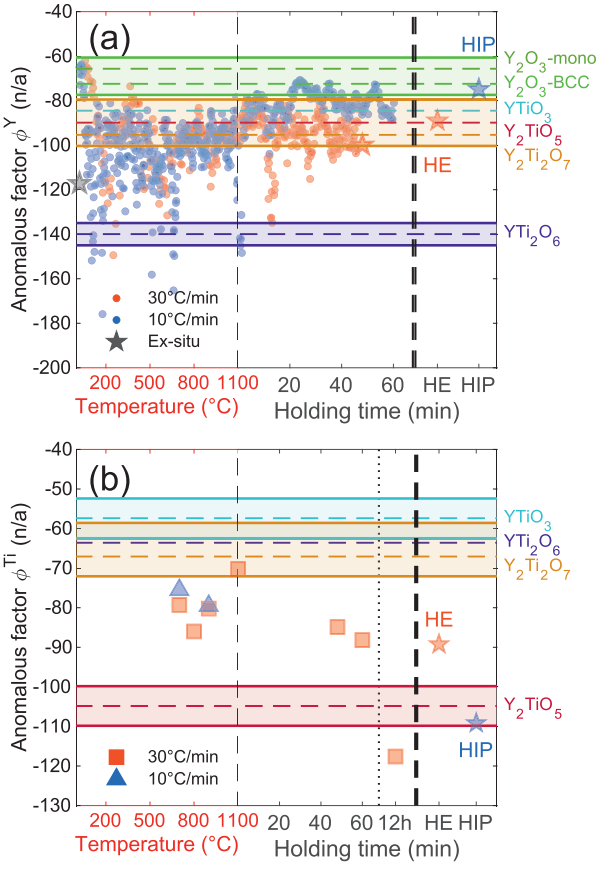

Fig. 6. Evolution of the anomalous factor at the Y K-edge acquired at the ESRF synchrotron (a) and at the Ti K-edge acquire at the PSI synchrotron (b), on CP-14Cr, HE-14Cr and HIP-14Cr specimens.

Fig. 6 plots the evolution of the ϕ^Y and ϕ^{Ti} anomalous factors [64], measured at the Y K-edge *in-situ* and ex-situ (Fig. 6a) and at the Ti K-edge, ex-situ only (Fig. 6b). These experimental data are compared to theoretical values of the anomalous factor for each precipitate displayed in colored dashed line and given in Tab. 3.

The evolution of the Y anomalous factor on the CP specimens heated either at 10 °C/min or at 30 °C/min appears to be very noisy at the beginning of the thermal treatment until a temperature between 800 and 1000 °C where the signal stabilizes around a value of -90 (Fig. 6a). This value could match with the phases $Y_2Ti_2O_7$, Y_2TiO_5 or $YTiO_3$ as their respective anomalous factor are too close

Table 3
Values of the mean atomic volume at RT for each considered phases along with the theoretical anomalous factors for precipitates – matrix couples.

Phases	Matrix	Y_2O_3- BCC	Y_2O_3- mono	$Y_2Ti_2O_7$	Y_2TiO_5	$YTiO_3$	YTi_2O_6
Vatm,ppt (Å3)	11.70	14.90	13.71	11.69	13.36	11.55	11.41
ϕ^Y	-	-71.4	-64.7	-93.6	-88.4	-82.9	-137.2
ϕ^{Ti}	-	-	-	-68.0	-165.8	-58.2	-20.4

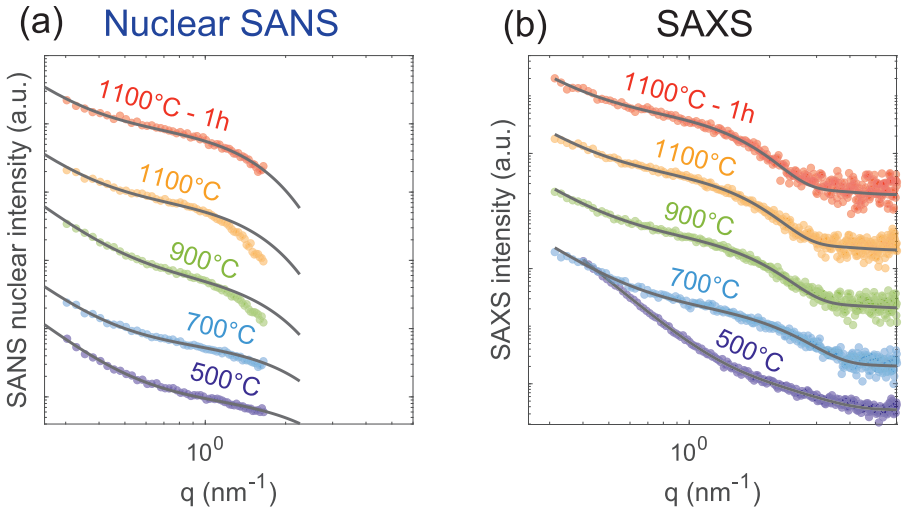

Fig. 7. Scattering intensity curves of the SANS measurements of the nuclear contribution (a), with the corresponding SAXS measurements used for the simultaneous fitting (a'), on CP specimens.

to be distinguished at the Y K-edge (regarding the residual noise after stabilization). The ex-situ measurements of the HE and HIP materials are in quite good agreement with the *in-situ* measurements of the CP specimens, eve although the HIP anomalous factor is slightly higher with a value close to -80.

For the measurements taken at the Ti K-edge, the theoretical anomalous factors of $Y_2Ti_2O_7$, Y_2TiO_5 and $YTiO_3$ can be distinguished more clearly thanks their significantly different Ti atomic fraction (Fig. 6b). Similarly to *in-situ* measurements, the anomalous factors experience significant noise during the heating ramp, so that it is difficult to know if *ex-situ* measurements are reliable below ~1000 °C. ϕ^{Ti} values are observed to decrease after the beginning of the isothermal annealing at 1100 °C, starting from a value fully consistent with $Y_2Ti_2O_7$ first, then in between $Y_2Ti_2O_7$ and Y_2TiO_5 after 1 h of ageing, and finally more consistent with Y_2TiO_5 after 12 h of annealing (taking into account that the YTi_2O_6 was excluded by the ϕ^Y analysis).

For the standard consolidation process, the HE anomalous factor lies in between $Y_2Ti_2O_7$ and Y_2TiO_5, which is in good agreement with the ϕ^{Ti} value on the CP material that followed a 30 °C/min heating and 1 h of isothermal holding at 1100 °C. The HIP value is however, close to the theoretical ϕ^{Ti} value of Y_2TiO_5, similar to the CP sample that followed a long annealing of 12 h at 1100 °C.

3.4. Small angle neutron scattering

The SANS and SAXS intensity curves acquired on the exact same specimens (SAXS measurements were performed on the samples measured by SANS) that followed interrupted thermal treatments and heating at 30 °C/min are displayed in Fig. 7. Experimental data were extracted thanks to a simultaneous least square fitting of both SANS (nuclear) and SAXS data, in order to share the same nano-oxides mean radius and dispersion, with all the other parameters fitted independently. The maximum of scattering vector q available for the SANS measurements was ~0.17 Å^{-1}, which is too low to distinguish the incoherent scattering present in the nuclear contribution of SANS intensity curves. The constant contribution of the model was then set to 0. This assumption will induce a slight overestimation of the fitted $\Delta\rho^2_{nuc} \times f_v$.

Table 4
Mean radius of precipitates in nm, fitted using both SANS and SAXS data, only SAXS and only SANS.

Mean radius (nm)	500 °C	700 °C	900 °C	1100 °C	1100 °C – 1 h
SAXS & SANS	0.72	0.88	1.12	1.24	1.29
SAXS only	0.66	0.88	1.12	1.23	1.27
SANS only	0.72	0.92	1.25	1.37	1.27

From the Fig. 7, the mean radius of precipitates that minimize both SAXS and SANS experimental patterns to the model have been determined, and are very close to the mean radius values fitting only SAXS and only SANS (nuclear). These data are presented in Tab. 4

The $\Delta\rho^2_{nuc} \times f_v$ evolution is displayed in Fig. 8. This evolution appears strictly decreasing for the SANS measurements before its stabilization between 900 °C and 1100 °C, whereas the SAXS measurements display an initial increment before decreasing (Fig. 2a and Fig. 3b). This change of behavior between SAXS and SANS $\Delta\rho^2 \times f_v$ evolution could be related to the chemistry of the nano-oxides, from which SANS and SAXS contrast do not have the same sensitivity.

The $\Delta\rho^2_{nuc} \times f_v$ extracted from SANS can then be compared to $\Delta\rho_{e^-} \times f_v$ extracted from SAXS. The ratio of these two values allows to get rid of the volume fraction dependency and then to get a chemical and structural information of the nano-oxides. Indeed, $\frac{\Delta\rho^2_{e^-}}{\Delta\rho^2_{nuc}}$ can be calculated theoretically with the knowledge of $\Delta\rho_{nuc}$ and $\Delta\rho_{e^-}$ for given matrix – precipitates couples, and compared to the experimental value, in a same way than the anomalous SAXS factor. An error bar has been calculated on the experimental ratios to take into account uncertainties on the effective thickness of the

Table 5
Theoretical contrast SAXS over SANS ratio values for the nuclear contrast.

Phases	Y_2O_3- BCC	Y_2O_3- mono	$Y_2Ti_2O_7$	Y_2TiO_5	$YTiO_3$	YTi_2O_6
$\frac{\Delta\rho^2_{e^-}}{\Delta\rho^2_{nuc}} \times 10^{-44}$	1.35	1.40	0.84	1.01	0.66	0.84

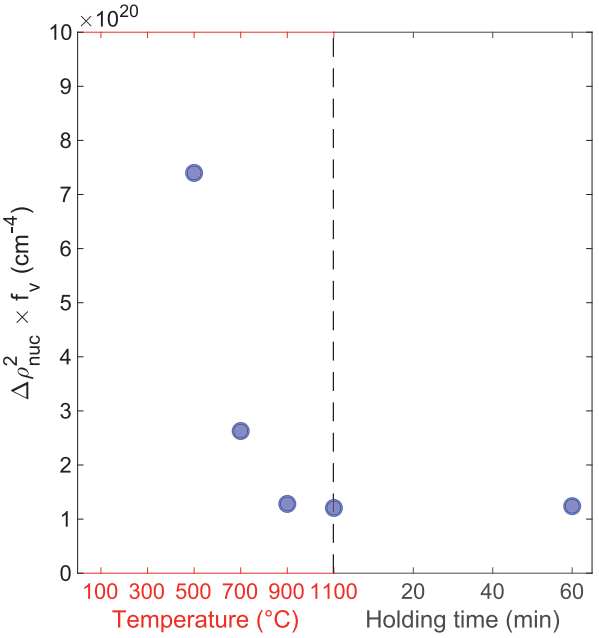

Fig. 8. Evolution of the SANS $\Delta\rho^2_{nuc} \times f_v$ on CP-14Cr specimens.

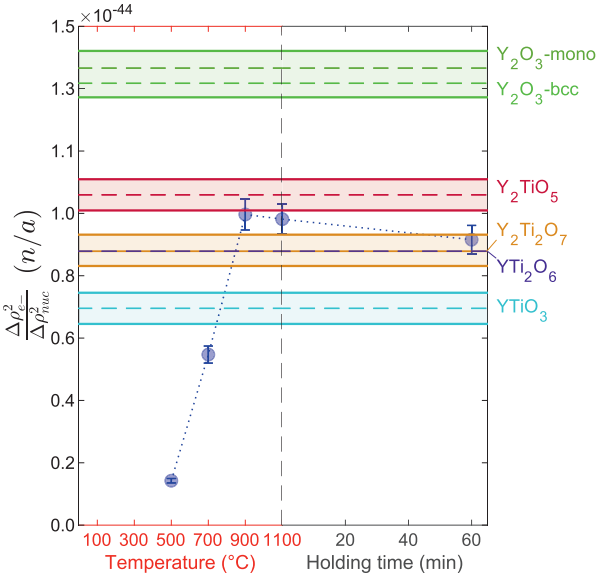

Fig. 9. Evolution of the contrast ratios of SAXS over SANS nuclear on CP-14Cr specimens.

specimens due to residual porosities after CP, calculated by taking into account a relative density of 80% ± 5%.

The evolution of this $\frac{\Delta\rho^2_{e^-}}{\Delta\rho^2_{nuc}}$ contrast ratio is displayed in Fig. 9. As for the anomalous factor, the experimental ratios are compared with theoretical contrast ratios displayed in colored dashed lines and given in Tab. 5. The contrast ratio starts at values matching with none of the theoretical ratios until 900 °C where it stabilizes between the theoretical ratios of Y_2TiO_5 and $Y_2Ti_2O_7$, which are also close to that of YTi_2O_6 (Fig. 9). From 900 °C to 1100 °C – 1 h annealing stage, the contrast ratio seems to slightly decrease, which would indicate an increase of the $Y_2Ti_2O_7$ volume fraction at the expense of the Y_2TiO_5. However, this decreasing tendency is highly unsure taking into account the significant estimated error and the absence of several measurements at each annealing stage. Moreover, an increase of the relative density of the CP specimens (*i.e.* decrease of the porosity) during annealing at 1100 °C would also result in such a decrease.

3.5. Atom probe tomography results

Slices from the APT reconstructed volumes for different interrupted thermal treatments are displayed in Fig. 10. On these reconstructions, Y, Ti and O are represented (in yellow, red and blue respectively) with the single ions and all the associated molecular ions. Throughout annealing, APT reveals the depletion of Y, Ti and O in solid solution leading to the formation of clearly defined nano-oxides with a high contrast either with the Y, Ti or O ions at 1100 °C and 1100 °C – 1 h. At the as-MA stage, clusters containing at least Y and O can be distinguished even if their contrast with the matrix is lower.

GBs were also present in some APT tips, several could be observed in the as-MA stage and few or none in the 900 °C and subsequent annealing stages (due to ongoing recovery and grain growth). The amount of visible GBs was obviously too low to perform a reliable statistical analysis. However, it could be noted that many of them were found enriched in W and Si, some in Ti and very few in C as displayed in supplementary material. These findings are in good agreement with Seol et al.'s work on the GBs segregation [74].

The number density of clusters was extracted by counting the clusters present in APT reconstructions (maximum separation method). These values of number density were then compared to the calculated number density of nano-oxides extracted from SAS (SAXS and SANS) measurements, based on the hypothesis of a precipitate – matrix couple ($Y_2Ti_2O_7$ pyrochlore – BCC Fe-14Cr) on Fig. 11; calculated by the following formula:

$$N^{Y_2Ti_2O_7\ -\ BCC} = \frac{f_v^{Y_2Ti_2O_7\ -\ BCC}}{\frac{4}{3}\pi R_m^3} \tag{8}$$

With $N^{Y_2Ti_2O_7\ -\ BCC}$ the number density with the given precipitate – matrix couple assumption and $f_v^{Y_2Ti_2O_7\ -\ BCC}$ calculated from:

$$f_v^{Y_2Ti_2O_7\ -\ BCC} = \frac{\left(\Delta\rho^2 \times f_v\right)_{exp}}{\Delta\rho^2_{Y_2Ti_2O_7\ -\ BCC}} \tag{9}$$

Where $(\Delta\rho^2 \times f_v)_{exp}$ can stand for $(\Delta\rho^2_{e^-} \times f_v)_{exp}$ extracted from SAXS experiments or $(\Delta\rho^2_{nuc} \times f_v)_{exp}$ extracted from SANS experiments (nuclear contrast).

Based on the hypothesis that the APT number density is reliable, any shift between APT and SAS number density reveals a bias from the hypothesis made on the precipitate structure and chemistry. At the beginning of the thermal treatment, a large discrepancy of around one order of magnitude can be observed between APT and SAXS data. This gap is even bigger between the APT and SANS number density at 500 °C. The SAXS and SANS agreement with APT improves from about 700 °C onwards. At the end of the heating ramp (1100 °C), the APT, SAXS and SANS number

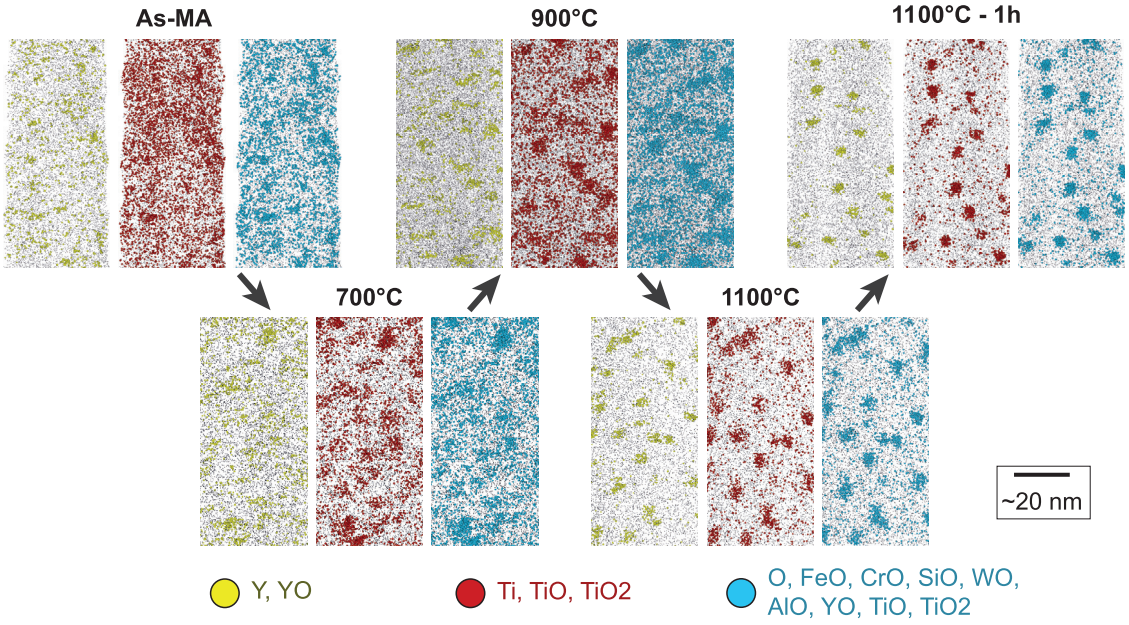

Fig. 10. About 10 nm thick slices of APT 3D reconstructions of the CP-14Cr specimen at different stages of the thermal treatment, from as-MA to 1100 °C – 1 h.

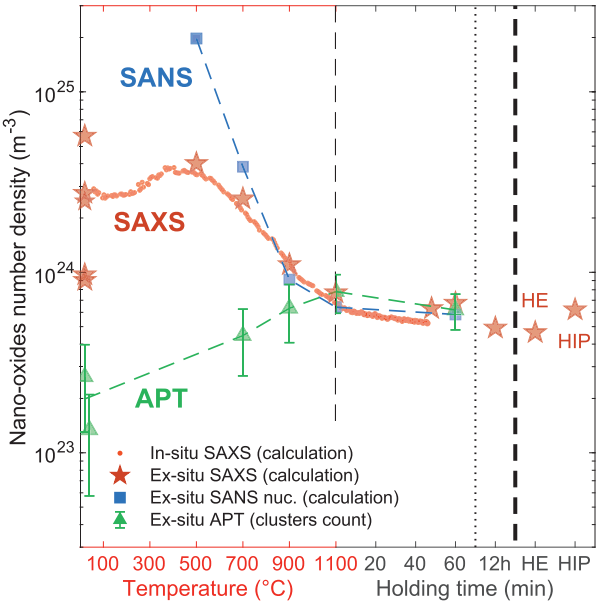

Fig. 11. Comparison of the evolution of the number density of nano-oxides calculated from SAS data and measured from APT data, in CP-14Cr, HE-14Cr and HIP-14Cr specimens.

densities are almost equal, which gives positive evidence for the $Y_2Ti_2O_7$ pyrochlore assumption after roughly 1000 °C. It should be noted, however, that the Y_2TiO_5 orthorhombic structure has a similar electronic density and can therefore not be ruled out by this comparison.

In addition, the SAXS number density values of HE and HIP materials are both very consistent with that of the CP specimens (from SAS and APT) after a thermal treatment up to 1100 °C – 1 h.

The evolution of chemical compositions analyzed from the APT tips are displayed in Fig. 12 for the elements Y, Ti, O and Al. As O quantification in APT is delicate, the absolute values of the O composition should be considered carefully as they are probably impacted by experimental bias. The error bars on the as-MA stage were calculated (standard deviation) from the 2 specimens available at this stage and gives an estimate of the experimental uncertainties on the compositions. All these graphs display two curves: the first representing the bulk composition (where only the GBs and surrounding affected volume were removed). The second (at lower or equal composition value) represent the chemical composition of the matrix only, extracted using the DIAM method. This leaves two distinct areas:

- the area between the bulk and the matrix composition represents the atoms inside the nano-oxides;
- the area below the DIAM matrix composition represents the residual solid solution.

The curves representing the bulk composition (upper curves) can be considered as constant for Y and O (Fig. 12a and Fig. 12c), whereas the Ti and Al bulk composition vary (Fig. 12b and Fig. 12d). The decrease of the Ti bulk composition can be explained by the formation of coarse Ti-rich precipitates such as titanium oxides or carbonitrides already observed in other studies in too low number density to be comprised in the APT volumes [44,53,75,76]. Moreover, Ti segregation can occur over the thermal treatment as Ti-enriched GBs were identified. The bulk composition of C (not represented here) is also decreasing, which is consistent with the precipitation of carbide phases (such as $M_{23}C_6$).

The quantity of solute atoms in the nano-oxides (area between the two curves) increases as expected throughout the thermal treatment. The amount of Y in the nano-oxides increases markedly around 1000 °C whereas the amount of Ti increases earlier, between the as-MA stage and 700 °C. At the end of the thermal treatment, the matrix solute content in all solutes is still substantial, with 0.034 at% Y and 0.12 at% Ti. The behavior of Al is more complex, with an as-MA stage where all the atoms are in solid solution, then clustering from 700 °C until 1100 °C, before both bulk and matrix compositions in Al come to almost 0 at 1100 °C – 1 h (Fig. 12d).

The analysis of PCFs (shown in supplementary material) allows to determine that Y, Ti and O are all present in the nano-oxides, from the as-MA stage. Therefore, the presence of Ti in the initial as-MA clusters, suspected thanks to the matrix and bulk compositions presented previously, is confirmed. Moreover, the PCF associated with Al demonstrates that the clustered Al atoms are contained into the Y-Ti-O nano-oxides between 700 °C and 1100 °C.

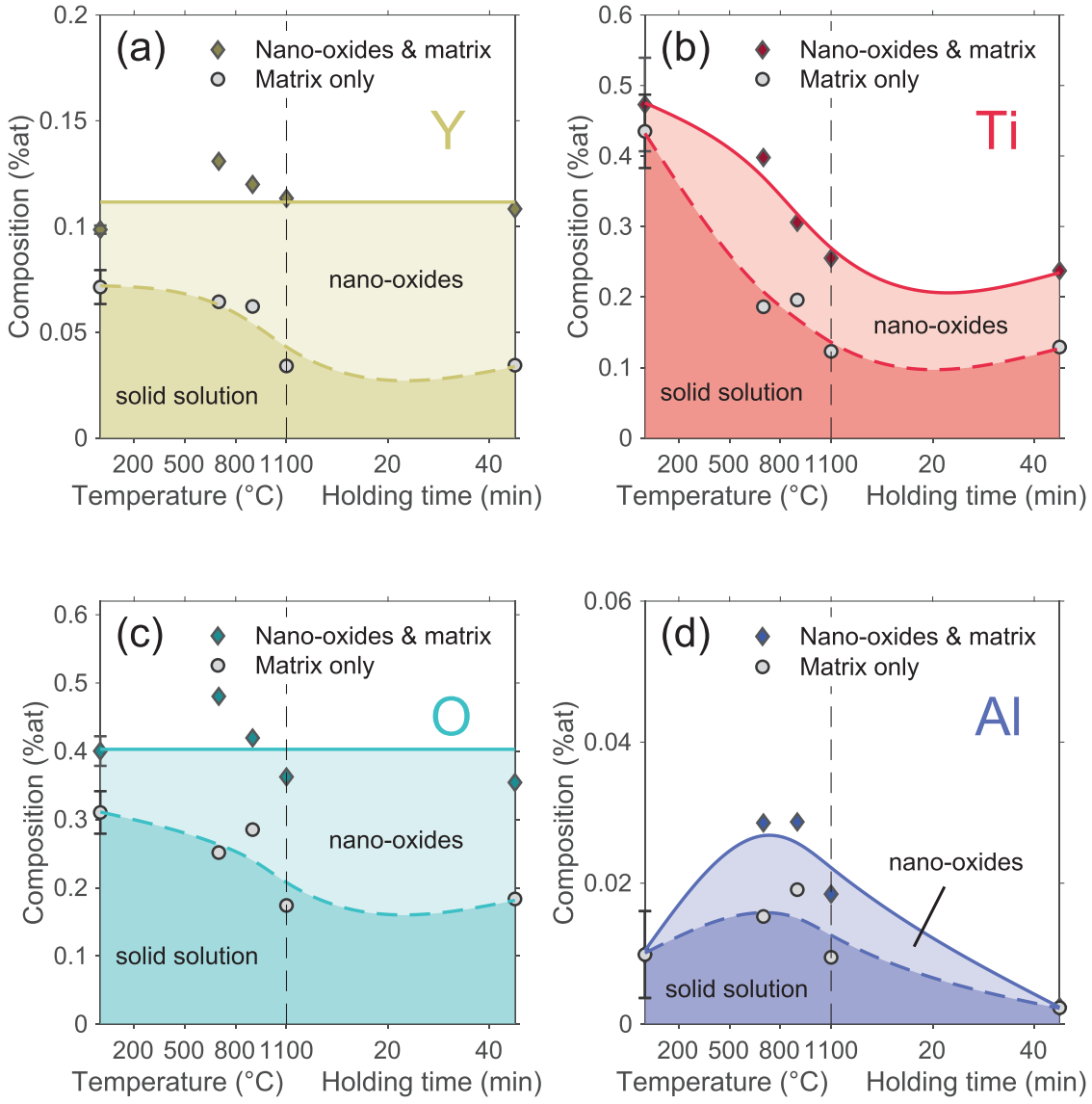

Fig. 12. Evolution of the matrix composition extracted by the DIAM method on CP-14Cr specimens for Y (a), Ti (b), O (c), and Al (d).

The mean radius of clusters measured by APT, extracted from the least square fit of the atoms auto-correlation of Y, Ti, O and Al are displayed and compared to the SAXS mean radius *in-situ* measurements in Fig. 13. A large discrepancy between APT and SAXS measurements appears clearly, with an APT mean radius approximately 2 times bigger than that from SAXS, even if the two values were extracted using the exact same lognormal distribution model. This difference can be explained by the APT effective spatial resolution which significantly increases the detected radius for very small precipitates [77].

4. Discussion

The experimental results presented previously reveal several features on the formation and evolution of the nano-precipitation in ferritic ODS steels:

(i) The presence of initial clusters at the as-MA stage, visible by SAXS measurements with high statistical reliability (Fig. 2 and Fig. 3) and by APT from direct observation of the reconstructed volumes (Fig. 10) and without any ambiguity from the PCF between atoms.

(ii) The significant changes in the chemistry and / or structure of the initial clusters becoming nano-oxides, highlighted by the comparison between SAS and APT measurements (Fig. 11), but also clearly visible with the contrast comparison between SAXS and SANS (Fig. 9), and the APT matrix composition (Fig. 12).

(iii) The outstanding thermal stability of nano-oxides in terms of size (Fig. 5) and number density (Fig. 11), along with a phase transformation of the nano-oxides from $Y_2Ti_2O_7$ to Y_2TiO_5 highlighted by SAXS measurements at the Ti K-edge (Fig. 6b).

4.1. As-MA initial clusters

4.1.1. Formation mechanism

Thanks to anomalous SAXS measurements at the Y K-edge, the presence of Y in the initial clusters has been demonstrated (Fig. 6a). This result is confirmed by the APT measurements, as the Y auto-correlation function clearly indicates the presence of Y-rich clusters (see supplementary material), also reflected in the gap between the matrix and bulk Y compositions of the APT volumes (Fig. 12). Anomalous SAXS at the Y K-edge also demonstrated that the electronic density of as-MA clusters is lower than that of the matrix. Since Y has a higher atomic number than Fe, this obser-

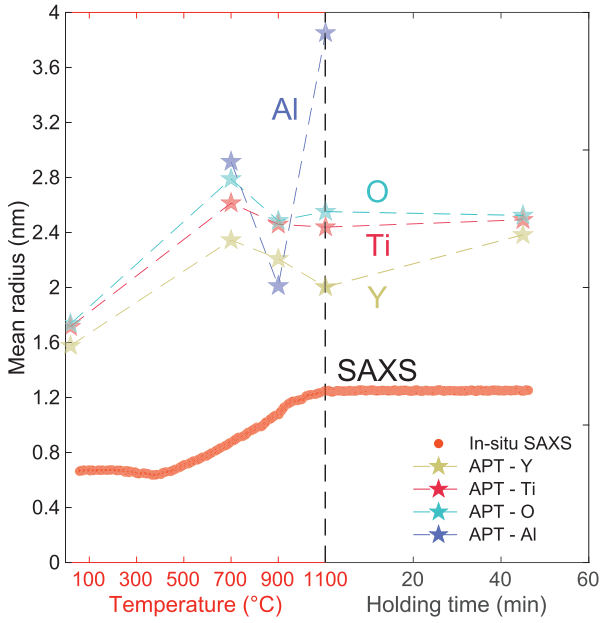

Fig. 13. Evolution of the mean radius of the nano-oxides extracted by APT (stars) and SAXS (dots) measurements on the CP-14Cr specimen.

vation could imply the presence of an element lighter than Fe in the clusters and / or a higher mean atomic volume for the clusters compared to the matrix. The presence of O (correlated to Y) in the clusters has been found thanks to the APT PCF, and can also be seen directly in the APT reconstructions (Fig. 10). A higher mean atomic volume of the as-MA clusters comparing to the matrix is also expected if they contain a significant concentration of vacancies, as predicted by ab-initio studies [27–30].

Ti has also been found in the as-MA clusters thanks to PCF from the APT measurements. The amount of Ti in these clusters is however believed to be lower than that of Y. Indeed, the difference between the bulk and the matrix compositions is small at this stage especially taking into account the error bars (Fig. 12), the signal to noise ratio of the Ti auto-correlation is also visibly lower than that of Y or O. Ab-initio studies tend to indicate that Y, Ti and O co-cluster with the help of the vacancies induced by MA. As the Y and O are introduced together (powder of Y_2O_3), separately from Ti (powder of TiH_2), Ti needs to diffuse towards the Y- and O-rich clusters, which can only happen by vacancy motion. This behavior could lead to a lower Ti content in the as-MA clusters. However, the presence of some Ti in the as-MA clusters demonstrates that these do not result only from breaking of Y_2O_3 particles.

4.1.2. Influence on the subsequent precipitation mechanism

The SAXS precipitates contribution seems to continuously evolve from the small as-MA clusters to bigger nano-oxides (Fig. 2 and Fig. 3). This suggests that the final nano-oxides grow from the as-MA clusters. This vision of a continuous transition is supported by the intermediate APT analysis which shows a progressive transformation from diffuse clustering to well defined objects. Yet, the number density of precipitates identified by APT measurements increases from the as-MA condition to the end of the thermal treatment by a factor ~×3. This increase requires the formation of new nuclei, principally between as-MA and 700 °C, where the number density already rises by a factor ~×2.2. The nucleation would then be completed before 900 °C, as the increase between as-MA and 900 °C is already ~×3.

Thus, the initial clusters introduced by the as-MA stage certainly play an important role in the spatial distribution and high number density of the final nano-oxides. Moreover, in case supplementary nucleation happens, it is certainly facilitated by the numerous point defects introduced by MA. MA should therefore not be only considered as a necessary processing step to obtain a supersaturated solid solution, but as a requirement to obtain a fine and homogeneous dispersion of nano-oxides after consolidation.

4.1.3. Chemical and structural evolution of the initial clusters to nano-oxides

The comparison of the SAS number density of nano-oxides with the APT number density (Fig. 11) clearly shows that before ~1000 °C, the precipitates are neither stoichiometric $Y_2Ti_2O_7$ pyrochlore nor Y_2TiO_5 orthorhombic. Indeed, the difference between the two values is around one order of magnitude, which cannot be attributed to APT detection issues. Even if cluster identification based on maximum distance separation methods is operator dependent, which could introduce fluctuation in the number density [80], the present system displays a high chemical contrast between the matrix (dilute Y, Ti and O concentration) and the nano-oxides (high concentration of Y, Ti and O), which tends to tighten the number density results between different operators. Thus, the discrepancy between APT and SAS number density is far too high to be only related to measurements uncertainties. This implies a significant evolution of the chemistry and / or structure of the nano-oxides between the as-MA and ~1000 °C stages.

The matrix and bulk chemical composition extracted from APT – not affected by reconstruction artefacts – evidence an increase of the proportion of atoms in the nano-oxides (area between the two curves Fig. 12), first for Ti (between as-MA and 700 °C) and then Y (between 900 °C and 1100 °C). This sequential composition evolution (Ti first, and Y afterwards) is consistent with the characteristic diffusion lengths along the thermal treatment (shown in supplementary material). It also implies an initial enrichment of clusters' chemical composition in Ti.

The behavior of Al during the nano-oxide precipitation sequence was also observed for the first time to our knowledge, even if other studies demonstrate the presence of Al in nano-oxides after consolidation [74,78,81]. In particular, Seol et al. discussed the formation mechanism of coarse (> 4 nm) core shell structures formed by an Al rich shell surrounding Y-Ti-O rich core observed by APT [74]. Al impurities are introduced by the MA process but is also an impurity present in the atomized powder and then is likely to be present in the majority of ODS steel grades of the literature. Y-Al rich oxides (like $YAlO_3$, $Y_4Al_2O_9$ or $Y_3Al_5O_{12}$) have lower enthalpy of formation [74] and are then predominant over Y-Ti-O oxides formation, as found experimentally by Kasada et al. [82]. However, the hypothesis that a high amount of Y-Al-O stoichiometric oxides are able to form is unlikely in our study due to the very low Al content of the steel, and as a matter of fact no Al-rich oxides were observed by APT in the 1100 °C – 1 h condition. Nano-oxides observed between 700 °C and 1100 °C are then more likely to be non-stoichiometric precipitates containing a small amount of Al. However, the decrease of the Al content in the nano-oxides with ageing times suggests the presence of coarser Al-Y rich oxides to which the Al initially present in the clusters could migrate. Several studies where Al was willfully introduced to increase the corrosion resistance [83,84], found that Al containing nano-oxides have a higher tendency to coarsen at high temperature than Y-Ti-O [66,85,82,47]. Therefore, the Al behavior observed in this study could have an influence on the precipitation kinetics, which would require a specific study to confirm.

When trying to reconcile the number densities of clusters obtained by SAS and by APT, which are very different from the as-MA stage up to roughly 1000 °C (Fig. 11), several effects can be considered (alone or in combination) as biases from our initial hypothesis of $Y_2Ti_2O_7$ pyrochlore precipitates:

i. presence of solvent Fe and/or Cr in the clusters;
ii. change of stoichiometry between the solutes Y, Ti and O;
iii. change of atomic volume due to a different structure or to the presence of vacancies.

The analysis of hypothesis -i- is complex: an enrichment of the clusters in Fe would result in an increase of both SAXS and SANS number density of clusters (as it would reduce the electronic and nuclear contrast). An enrichment in Cr would result in the increase of SAXS number density but a decrease of SANS number density, reducing the gap between SAXS and SANS but increasing the gap between SAS and APT. Therefore, even if the presence of Fe and Cr cannot be completely ruled out, it can clearly not explain the discrepancy between APT and SAS. The hypothesis -ii- is favorable to an enrichment of light elements in the clusters (O and Ti) that lower the SAS number density of clusters, up to a certain extent in accordance with anomalous SAXS at the Y K-edge and Ti K-edge. The hypothesis -iii- can lead to a significant reduction of the SAS number density of clusters by increasing the atomic volume of the clusters (*i.e.* assuming a structural modification and presence of vacancies in the clusters).

A combination of the hypothesis -ii- and -iii- would therefore contribute to reduce the gap between APT and SAS number density of nano-oxides. However, fitting the two number densities was found impossible without introducing an unrealistic (too high) density of vacancies in the nano-oxides below ~800 °C. This discrepancy could finally arise from the chosen SAS interpretation model, consisting in a lognormal distribution of spheres. Indeed, in the first stages of clustering, such a model does not describe the microstructure realistically. Another model could be used, describing the microstructure as spatial chemical fluctuations instead of spherical precipitates [86,87]. This model is probably more adapted to the description of these early stages of precipitation. However, this model does not allow extracting the number density of clusters, and therefore the comparison performed between APT and SAS data should also be revised.

4.1.4. Nature and stability of the nano-oxides during 1100 °C isothermal holding

The nano-oxides display an outstanding resistance to coarsening at 1100 °C, even after 12 h of isothermal holding, without a noticeable increase of mean radius, as shown in Fig. 5. The stabilization of the nano-oxides into a near-stoichiometric and structured compound can be expected to play an important role in this stabilization. Indeed, the mean radius tends to stabilize just before the end of the heating ramp around 1000 °C, simultaneously with the nano-oxides stoichiometry and structural stabilization, as demonstrated previously (Fig. 6, Fig. 9a and Fig. 11).

At 1100 °C, anomalous SAXS measurements at the Ti K-edge, realized for the first time to our knowledge in the present study, allow to determine that the majority of nano-oxides are near-stoichiometric $Y_2Ti_2O_7$ pyrochlore (also containing a small amount of Al as indicated by APT). After 1 h of isothermal holding at this temperature, the evolution of the Ti anomalous factor indicates the simultaneous presence of $Y_2Ti_2O_7$ and Y_2TiO_5 nano-oxides in similar volume fraction. After 12 h of annealing time, the Ti experimental anomalous factor is just below the Y_2TiO_5 theoretical factor. This shift from the theoretical value, can be due to experimental uncertainty or some bias from stoichiometry within the Y_2TiO_5 phase (it could be explained by a $Y_2Ti_{0.9}O_5$ composition of the oxides). This phase transformation of the nano-oxides from $Y_2Ti_2O_7$ to Y_2TiO_5 is in good agreement with the findings of Kim et al. who observed by XRD the appearance of Y_2TiO_5 orthorhombic phase after 4 h of annealing at 1150 °C with an increasing volume fraction with annealing time [23]. It should be noted however that, as only one specimen has been measured after 12 h of annealing, the repeatability of this result is not ensured and would therefore require further experiments to be fully confirmed. Due to some measurements limitation (uncertainty on the porosity and lack of incorporation of the incoherent scattering) and closeness of the $Y_2Ti_2O_7$ and Y_2TiO_5 contrast ratios, The SAXS over SANS (nuclear) contrast ratio has not been found relevant enough to be able to discriminate between $Y_2Ti_2O_7$ and Y_2TiO_5.

The Ti anomalous factor of the HE material matches with that of the CP material after 1100 °C – 1 h ageing following a 30 °C/min ramp (Fig. 6b). This consistency can be attributed to the similar thermal treatment applied to the CP and the HE specimens (for the latter, heating ramp at around 40 °C/min, ~45 min of isothermal at 1100 °C followed by final heating of 1 h at 1050 °C). The HIP anomalous factor is consistent with the CP material aged at 1100 °C – 12 h, but slightly higher, matching with the Y_2TiO_5 theoretical anomalous factor. This similarity can arise from the longer time spent by HIP specimens at high temperature (following a ~5 °C/min heating followed by 2 h at 1100 °C before a slow cooling at ~5 °C/min). This longer annealing could therefore represent enough time to complete the $Y_2Ti_2O_7 \rightarrow Y_2TiO_5$ phase transformation of the nano-oxides, like in the 12 h annealed CP material. It can be observed however that Oono et al. do not detect Y_2TiO_5 after 4 h of isothermal treatment at 1150 °C [24]. This phase transformation of the nano-oxides with annealing time is then certainly a common trend but could appear at different rates depending on the ODS steel design (such as differences in chemical composition in Ti or minor alloying elements that are known to precipitate with Ti) and the fabrication process.

The matrix composition measured by APT is very stable from 1100 °C to 1100 °C – 1 h, which implies that no Y enrichment of the nano-oxides occurs in this time range. Unfortunately, no APT data at 12 h is available, however the transformation of the nano-oxides from $Y_2Ti_2O_7$ to Y_2TiO_5 should result in the nano-oxides enrichment in Y and O coming from the solid solution or a release of Ti contained in the nano-oxides through the matrix, coarse precipitates, or GBs. Ti enrichment at GBs has been observed in this study and in other studies [74,88]. It is important to note that the nano-oxides phase transformation does not affect the coarsening rate, which remains extremely low as demonstrated by the SAXS analysis.

At the end of the thermal treatment (1100 °C – 1 h), the Y in solid solution is measured by APT around 0.03 at%, which is much higher than the solubility limit at room temperature but in good agreement with the solubility limit at 1100 °C. Indeed, according to Farkas et al. this solubility limit is 0.075 at% at 1320 °C [89] and 0.011 at% at 800 °C according to Epstein [90]. In the literature several studies also display a similar composition of Y in the matrix of similar ODS steels, determined by APT [25,91,92]. This Y matrix composition can thus be explained by the fast cooling of the CP and HE specimens.

The HIP specimens followed however a slow cooling (~5 °C/min), and even if the APT matrix composition of this specimen is not available, the $\Delta\rho_{e^-}^2 \times f_v$ value is higher, which can be translated – at a constant nano-oxide nature – into a higher volume fraction of nano-oxides. This f_v increment can thus be related to the (full or partial) precipitation of the 0.03 at% Y remaining in solid solution at high temperature. Indeed, the calculation of the volume fraction increase induced by the precipitation of the residual 0.03 at% Y is consistent with the volume fraction measured by SAXS on the HIP material.

In order to give a global overview of the key points discussed previously, a scheme describing the precipitation evolution in terms of kinetics, chemical and structural evolution of the nano-oxides from the as-MA to consolidated stages is represented in Fig. 14.

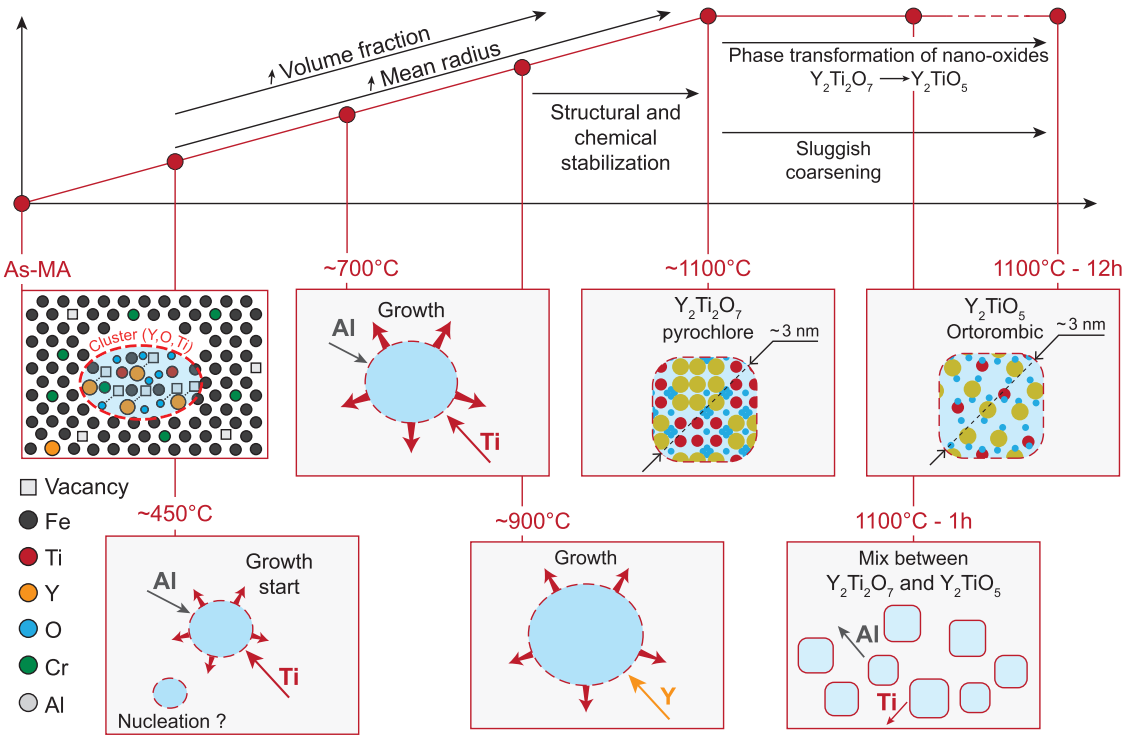

Fig. 14. Scheme outlining the major chemical and structural evolution of the nano-oxides identified throughout the thermal treatment of ODS steels fabrication process.

5. Conclusion

A multi-technique characterization of the evolution of the chemical and structural characteristics of the nano-oxides throughout the consolidation process of ODS ferritic steel has been performed. Thanks to comparisons between all the techniques used, several key features have been established:

(i) Small sub-nanometric clusters are present at the as-MA stage, containing not only Y and O but also Ti (probably in lesser extent).
(ii) The as-MA clusters start growing at ~450 °C, and then their volume fraction increases along with some further nucleation.
(iii) The nano-oxides become enriched in Ti and Al between as-MA and 700 °C and then in Y between 900 °C and 1100 °C. This two steps diffusion (Al and Ti and then Y) is consistent with the diffusion coefficient of those elements.
(iv) The stoichiometry and structure of the nano-oxides stabilizes around 1000 °C to reach a majority of $Y_2Ti_2O_7$ pyrochlore phase measured at 1100 °C.
(v) The nano-oxides transform from a majority of $Y_2Ti_2O_7$ to a nearly equal volume fraction of $Y_2Ti_2O_7$ and Y_2TiO_5 after 1 h of isothermal at 1100 °C. This isothermal holding time also seems sufficient to achieve the migration of the Al out of the nano-oxides.
(vi) $Y_2Ti_2O_7$ transforms fully into Y_2TiO_5 after a long annealing time (12 h) at 1100 °C. This transformation however induces no increase of the coarsening rate of the nano-oxides, suggesting that both oxide phases ($Y_2Ti_2O_7$ and Y_2TiO_5) are extremely stable.

Declaration of Competing Interest

The authors declare that they have no known competing financial interests or personal relationships that could have appeared to influence the work reported in this paper.

Acknowledgements

The authors acknowledge Nathalie Boudet, Nils Blanc, Gilbert Chahine and Stephan Arnaud from D2AM-BM02 beamline at the ESRF synchrotron for the in- and ex-situ anomalous SAXS measurement at the Y K-edge. Authors also strongly thanks Denis Menut of the MARS beamline at the SOLEIL synchrotron for invaluable testing of anomalous SAXS measurements at the Ti K-edge and his help with the PSI experiments. We acknowledge Andreas Menzel and the cSAXS beamline team at PSI – SLS synchrotron for the anomalous SAXS measurements at the Ti K-edge and help provided with the data processing. We also thank Marie-Helene Mathon for the SANS measurements at the PAXY beamline of the nuclear reactor ORPHEE. This work received assistance from the “Agence Nationale de la Recherche” program GENESIS referenced as ANR-11-EQPX-0020. This research was founded by the Reactors of 4th Generation (R4G) program of the French Alternative Energies and Atomic Energy Commission (CEA).

Supplementary materials

Supplementary material associated with this article can be found, in the online version, at doi:10.1016/j.actamat.2022.117992.

References

[1] S. Ukai, S. Ohtsuka, T. Kaito, Y. de Carlan, J. Ribis, J. Malaplate, Oxide dispersion-strengthened/ferrite-martensite steels as core materials for Generation IV nuclear reactors, 2017.
[2] S.J. Zinkle, J.L. Boutard, D.T. Hoelzer, A. Kimura, R. Lindau, G.R. Odette, M. Rieth, L. Tan, H. Tanigawa, Development of next generation tempered and ODS reduced activation ferritic/martensitic steels for fusion energy applications, Nuclear Fusion 57 (2017) 092005, doi:10.1088/1741-4326/57/9/092005.
[3] P. Yvon, M.L. Flem, C. Cabet, J.L. Seran, Structural materials for next generation nuclear systems: Challenges and the path forward, Nuclear Engineering and Design 294 (2015) 161–169, doi:10.1016/j.nucengdes.2015.09.015.
[4] P. Dubuisson, Y. de Carlan, V. Garat, M. Blat, ODS Ferritic/martensitic alloys for Sodium Fast Reactor fuel pin cladding, Journal of Nuclear Materials 428 (2012) 6–12, doi:10.1016/j.jnucmat.2011.10.037.

[5] T. Tanno, M. Takeuchi, S. Ohtsuka, T. Kaito, Corrosion behavior of ODS steels with several chromium contents in hot nitric acid solutions, Journal of Nuclear Materials 494 (2017) 219–226, doi:10.1016/j.jnucmat.2017.07.008.

[6] B. Gwinner, M. Auroy, D. Mas, A. Saint-Jevin, S. Pasquier-Tilliette, Impact of the use of the ferritic/martensitic ODS steels cladding on the fuel reprocessing PUREX process, Journal of Nuclear Materials 428 (2012) 110–116, doi:10.1016/j.jnucmat.2011.11.005.

[7] J. Ribis, M.-L. Lescoat, S.Y. Zhong, M.-H. Mathon, Y. de Carlan, Influence of the low interfacial density energy on the coarsening resistivity of the nano-oxide particles in Ti-added ODS material, Journal of Nuclear Materials 442 (2013) S101-S105, doi:10.1016/j.jnucmat.2012.10.051.

[8] J. Ribis, M.A. Thual, T. Guilbert, Y. De Carlan, A. Legris, Relaxation path of metastable nanoclusters in oxide dispersion strengthened materials, Journal of Nuclear Materials 484 (2017) 183–192, doi:10.1016/j.jnucmat.2016.12.007.

[9] M. Praud, F. Mompiou, J. Malaplate, D. Caillard, J. Garnier, A. Steckmeyer, B. Fournier, Study of the deformation mechanisms in a Fe-14% Cr ODS alloy, Journal of Nuclear Materials 428 (2012) 90–97, doi:10.1016/j.jnucmat.2011.10.046.

[10] M. Dadé, J. Malaplate, J. Garnier, F. Barcelo, F. Mompiou, P. Wident, A. Deschamps, Influence of temperature and strain rate on the deformation and damage mechanisms of oxide dispersion strengthened ferritic steels, Materialia 4 (2018) 585–594, doi:10.1016/j.mtla.2018.11.016.

[11] S. Ukai, T. Okuda, M. Fujiwara, T. Kobayashi, S. Mizuta, H. Nakashima, Characterization of High Temperature Creep Properties in Recrystallized 12Cr-ODS Ferritic Steel Claddings, Journal of Nuclear Science and Technology 39 (2002) 872–879, doi:10.1080/18811248.2002.9715271.

[12] S. Ukai, M. Fujiwara, Perspective of ODS alloys application in nuclear environments, Journal of Nuclear Materials (2002) 749–757 307-311, doi:10.1016/S0022-3115(02)01043-7.

[13] T. Stan, Y. Wu, J. Ciston, T. Yamamoto, G.R. Odette, Characterization of polyhedral nano-oxides and helium bubbles in an annealed nanostructured ferritic alloy, Acta Materialia 183 (2020) 484–492, doi:10.1016/j.actamat.2019.10.045.

[14] L. Yang, Y. Jiang, G.R. Odette, T. Yamamoto, Z. Liu, Y. Liu, Trapping helium in Y2Ti2O7 compared to in matrix iron: A first principles study, Journal of Applied Physics 115 (2014), doi:10.1063/1.4871282.

[15] C. Suryanarayana, Mechanical alloying and milling, Progress in Materials Science 46 (2001) 1–184, doi:10.1016/S0079-6425(99)00010-9.

[16] B. Dousti, R. Mojaver, H. Reza, R. Sarraf, Microstructural evolution and chemical redistribution in Fe-Cr-W-Ti-Y_2O_3 nanostructured powders prepared by ball milling, Journal of Alloys and Compounds 577 (2013) 409–416, doi:10.1016/j.jallcom.2013.05.201.

[17] M.J. Alinger, G.R. Odette, D.T. Hoelzer, On the role of alloy composition and processing parameters in nanocluster formation and dispersion strengthening in nanostuctured ferritic alloys, Acta Materialia 57 (2009) 392–406, doi:10.1016/j.actamat.2008.09.025.

[18] P. He, J. Hoffmann, A. Möslang, Effect of milling time and annealing temperature on nanoparticles evolution for 13.5% Cr ODS ferritic steel powders by joint application of XAFS and TEM, Journal of Nuclear Materials 501 (2018) 381–387, doi:10.1016/j.jnucmat.2018.01.021.

[19] M. Saber, W. Xu, L. Li, Y. Zhu, C.C. Koch, R.O. Scattergood, Size effect of primary Y2O3 additions on the characteristics of the nanostructured ferritic ODS alloys: Comparing as-milled and as-milled/annealed alloys using S/TEM, Journal of Nuclear Materials 452 (2014) 223–229, doi:10.1016/j.jnucmat.2014.05.014.

[20] L.L. Hsiung, M.J. Fluss, S.J. Tumey, B.W. Choi, Y. Serruys, F. Willaime, A. Kimura, Formation mechanism and the role of nanoparticles in Fe-Cr ODS steels developed for radiation tolerance, Physical Review B - Condensed Matter and Materials Physics 82 (2010) 1–13, doi:10.1103/PhysRevB.82.184103.

[21] L. Toualbi, M. Ratti, G. André, Y. De Carlan, F. Onimus, Use of neutron and X-ray diffraction to study the precipitation mechanisms of oxides in ODS materials, Journal of Nuclear Materials 417 (2011) 225–228, doi:10.1016/j.jnucmat.2010.12.071.

[22] L. Dai, Y. Liu, Z. Dong, Size and structure evolution of yttria in ODS ferritic alloy powder during mechanical milling and subsequent annealing, Powder Technology 217 (2012) 281–287, doi:10.1016/j.powtec.2011.10.039.

[23] S.W. Kim, T. Shobu, S. Ohtsuka, T. Kaito, M. Inoue, M. Ohnuma, Kinetic approach for growth and coalescence of nano-size oxide particles in 9Cr-ODS steel using high-energy synchrotron radiation X-rays in SPring-8, Materials Transactions 50 (2009) 917–921, doi:10.2320/matertrans.MER2008439.

[24] N. Oono, S. Ukai, Precipitation of Oxide Particles in Oxide Dispersion Strengthened (ODS) Ferritic Steels, Materials Transactions 59 (2018) 1651–1658, doi:10.2320/matertrans.M2018110.

[25] C.A. Williams, P. Unifantowicz, N. Baluc, G.D.W. Smith, E.A. Marquis, The formation and evolution of oxide particles in oxide-dispersion-strengthened ferritic steels during processing, Acta Materialia 61 (2013) 2219–2235, doi:10.1016/j.actamat.2012.12.042.

[26] C.A. Williams, D. Haley, E.A. Marquis, G.D.W. Smith, M.P. Moody, Defining clusters in APT reconstructions of ODS steels, Ultramicroscopy 132 (2013) 271–278, doi:10.1016/j.ultramic.2012.12.011.

[27] J.-L. Bocquet, C. Barouh, C.-C. Fu, Migration mechanism for oversized solutes in cubic lattices: The case of yttrium in iron, Physical Review B 95 (2017), doi:10.1103/PhysRevB.95.214108.

[28] C.L. Fu, M. Krčmar, G.S. Painter, X.Q. Chen, Vacancy mechanism of high oxygen solubility and nucleation of stable oxygen-enriched clusters in Fe, Physical Review Letters 99 (2007) 1–4, doi:10.1103/PhysRevLett.99.225502.

[29] Y.A. Mastrikov, M.N. Sokolov, S. Koch, Y.F. Zhukovskii, A. Gopejenko, P.V. Vladimirov, V.A. Borodin, E.A. Kotomin, A. Möslang, Ab initio modelling of the initial stages of the ODS particle formation process, Nuclear Instruments and Methods in Physics Research Section B: Beam Interactions with Materials and Atoms 435 (2018) 70–73, doi:10.1016/j.nimb.2018.01.022.

[30] D. Murali, B.K. Panigrahi, M.C. Valsakumar, S. Chandra, C.S. Sundar, B. Raj, The role of minor alloying elements on the stability and dispersion of yttria nanoclusters in nanostructured ferritic alloys: An ab initio study, Journal of Nuclear Materials 403 (2010) 113–116, doi:10.1016/j.jnucmat.2010.06.008.

[31] M.K. Miller, C.L. Fu, M. Krcmar, D.T. Hoelzer, C.T. Liu, Vacancies as a constitutive element for the design of nanocluster- strengthened ferritic steels, Frontiers of Materials Science in China 3 (2009) 9–14, doi:10.1007/s11706-009-0001-8.

[32] A. Gopejenko, Y.F. Zhukovskii, P.V. Vladimirov, E.A. Kotomin, A. Möslang, Ab initio simulation of yttrium oxide nanocluster formation on fcc Fe lattice, Journal of Nuclear Materials 406 (2010) 345–350, doi:10.1016/j.jnucmat.2010.09.005.

[33] A. Claisse, P. Olsson, First-principles calculations of (Y, Ti, O) cluster formation in body centred cubic iron-chromium, Nuclear Instruments and Methods in Physics Research, Section B: Beam Interactions with Materials and Atoms 303 (2013) 18–22, doi:10.1016/j.nimb.2013.01.016.

[34] V. Badjeck, M.G. Walls, L. Chaffron, J. Malaplate, K. March, New insights into the chemical structure of Y2Ti2O7-δ nanoparticles in oxide dispersion-strengthened steels designed for sodium fast reactors by electron energy-loss spectroscopy, Journal of Nuclear Materials 456 (2015) 292–301, doi:10.1016/j.jnucmat.2014.09.058.

[35] J. Ribis, Y. De Carlan, Interfacial strained structure and orientation relationships of the nanosized oxide particles deduced from elasticity-driven morphology in oxide dispersion strengthened materials, Acta Materialia 60 (2012) 238–252, doi:10.1016/j.actamat.2011.09.042.

[36] Y. Wu, J. Ciston, S. Kräemer, N. Bailey, G.R. Odette, P. Hosemann, The crystal structure, orientation relationships and interfaces of the nanoscale oxides in nanostructured ferritic alloys, Acta Materialia 111 (2016) 108–115, doi:10.1016/j.actamat.2016.03.031.

[37] S. Ohtsuka, S. Ukai, M. Fujiwara, T. Kaito, T. Narita, Improvement of 9Cr-ODS martensitic steel properties by controlling excess oxygen and titanium contents, Journal of Nuclear Materials (2004) 372–376 329-333, doi:10.1016/j.jnucmat.2004.04.043.

[38] S. Yamashita, S. Ohtsuka, N. Akasaka, S. Ukai, S. Ohnuki, Formation of nanoscale complex oxide particles in mechanically alloyed ferritic steel, Philosophical Magazine Letters 84 (2004) 525–529, doi:10.1080/09500830412331303609.

[39] A.J. London, S. Santra, S. Amirthapandian, B.K. Panigrahi, R.M. Sarguna, S. Balaji, R. Vijay, C.S. Sundar, S. Lozano-Perez, C.R.M. Grovenor, Effect of Ti and Cr on dispersion, structure and composition of oxide nano-particles in model ODS alloys, Acta Materialia 97 (2015) 223–233, doi:10.1016/j.actamat.2015.06.032.

[40] A.J. London, S. Lozano-Perez, M.P. Moody, S. Amirthapandian, B.K. Panigrahi, C.S. Sundar, C.R.M. Grovenor, Quantification of oxide particle composition in model oxide dispersion strengthened steel alloys, Ultramicroscopy 159 (2015) 360–367, doi:10.1016/j.ultramic.2015.02.013.

[41] C. Hatzoglou, B. Radiguet, P. Pareige, Experimental artefacts occurring during atom probe tomography analysis of oxide nanoparticles in metallic matrix: Quantification and correction, Journal of Nuclear Materials 492 (2017) 279–291, doi:10.1016/j.jnucmat.2017.05.008.

[42] M. Ohnuma, J. Suzuki, S. Ohtsuka, S.W. Kim, T. Kaito, M. Inoue, H. Kitazawa, A new method for the quantitative analysis of the scale and composition of nanosized oxide in 9Cr-ODS steel, Acta Materialia 57 (2009) 5571–5581, doi:10.1016/j.actamat.2009.07.054.

[43] A. Hirata, T. Fujita, Y.R. Wen, J.H. Schneibel, C.T. Liu, M.W. Chen, Atomic structure of nanoclusters in oxide-dispersion-strengthened steels, Nature Materials 10 (2011) 922–926, doi:10.1038/nmat3150.

[44] M.K. Miller, C.M. Parish, Q. Li, Advanced oxide dispersion strengthened and nanostructured ferritic alloys, Materials Science and Technology 29 (2013) 1174–1178, doi:10.1179/1743284713Y.0000000207.

[45] A.J. London, S. Lozano-Perez, S. Santra, S. Amirthapandian, B.K. Panigrahi, C.S. Sundar, C.R.M. Grovenor, Comparison of atom probe tomography and transmission electron microscopy analysis of oxide dispersion strengthened steels, Journal of Physics: Conference Series 522 (2014) 012028, doi:10.1088/1742-6596/522/1/012028.

[46] P. Unifantowicz, T. Płociński, C.A. Williams, R. Schäublin, N. Baluc, Structure of complex oxide nanoparticles in a Fe-14Cr-2W-0.3Ti-0.3Y2O3ODS RAF steel, Journal of Nuclear Materials 442 (2013) 158–163, doi:10.1016/j.jnucmat.2013.04.048.

[47] S. Ukai, H. Okada, M. Inoue, T. Nishida, M. Fujiwara, S. Nomura, S. Shikakura, K. Asabe, Alloying design of oxide dispersion for long life FBRs core materials strengthened ferritic steel, Journal of Nuclear Materials 204 (1993) 5–73, doi:10.1016/0022-3115(93)90200-I.

[48] Q.J. Li, L.M. Xu, C. Fan, F.B. Zhang, Y.Y. Lv, B. Ni, Z.Y. Zhao, X.F. Sun, Single crystal growth of the pyrochlores R2Ti2O7 (R=rare earth) by the optical floating-zone method, Journal of Crystal Growth 377 (2013) 96–100, doi:10.1016/j.jcrysgro.2013.04.048.

[49] P. Jegadeesan, S. Amirthapandian, G. Kaur, S. Chandra, B.K. Panigrahi, Characterization of M-O bonds in Y2Ti2O7 and Y2TiO5 with EELS, Physica Status Solidi (B) 252 (2015) 206–211, doi:10.1002/pssb.201451297.

[50] D. Chen, D. Yin, J. Zhou, X. Lin, H. Zhang, N. Shi, The Discovery Of An End Member Of The (Y)-Aeschynite Group - (Ti, Y)-Aeschynite, Geological Review (Beijing) 40 (1994) 82–86.

[51] I.A. Kibalin, Z. Yan, A.B. Voufack, S. Gueddida, B. Gillon, A. Gukasov, F. Porcher, A.M. Bataille, F. Morini, N. Claiser, M. Souhassou, C. Lecomte, J.-M. Gillet, M. Ito, K. Suzuki, H. Sakurai, Y. Sakurai, C.M. Hoffmann, X.P. Wang, Spin density in YTiO 3 : I. Joint refinement of polarized neutron diffraction and magnetic x-ray diffraction data leading to insights into orbital ordering, Physical Review B 96 (2017), doi:10.1103/PhysRevB.96.054426.

[52] H. Yusa, T. Tsuchiya, N. Sata, Y. Ohishi, Dense Yttria Phase Eclipsing the A-Type Sesquioxide Structure: High-Pressure Experiments and ab initio Calculations, Inorganic Chemistry 49 (2010) 4478–4485, doi:10.1021/ic100042z.

[53] H. Sakasegawa, L. Chaffron, F. Legendre, L. Boulanger, T. Cozzika, M. Brocq, Y. De Carlan, Correlation between chemical composition and size of very small oxide particles in the MA957 ODS ferritic alloy, Journal of Nuclear Materials 384 (2009) 115–118, doi:10.1016/j.jnucmat.2008.11.001.

[54] M.K. Miller, K.F. Russell, D.T. Hoelzer, Characterization of precipitates in MA/ODS ferritic alloys, Journal of Nuclear Materials 351 (2006) 261–268, doi:10.1016/j.jnucmat.2006.02.004.

[55] M. Yamamoto, S. Ukai, S. Hayashi, T. Kaito, S. Ohtsuka, Formation of residual ferrite in 9Cr-ODS ferritic steels, Materials Science and Engineering: A 527 (2010) 4418–4423, doi:10.1016/j.msea.2010.03.079.

[56] M. Yamamoto, S. Ukai, S. Hayashi, T. Kaito, S. Ohtsuka, Reverse phase transformation from α to γ in 9Cr-ODS ferritic steels, Journal of Nuclear Materials 417 (2011) 237–240, doi:10.1016/j.jnucmat.2010.12.250.

[57] J. Zhang, Y. Li, F. Bao, X. Rui, Z. Duan, W. Yan, Q. Shi, W. Wang, Y. Shan, K. Yang, Study on the formation mechanism of Y-Ti-O oxides during mechanical milling and annealing treatment, Advanced Powder Technology 32 (2021) 582–590, doi:10.1016/j.apt.2021.01.005.

[58] P. He, P. Gao, Q. Tian, J. Lv, W. Yao, An in situ SANS study of nanoparticles formation in 9Cr ODS steel powders, Materials Letters 209 (2017) 535–538, doi:10.1016/j.matlet.2017.08.051.

[59] A. Deschamps, F.D. Geuser, J. Malaplate, D. Sornin, When do oxide precipitates form during consolidation of oxide dispersion strengthened steels? Journal of Nuclear Materials 482 (2016) 83–87, doi:10.1016/j.jnucmat.2016.10.017.

[60] G. Spartacus, J. Malaplate, F. De Geuser, D. Sornin, A. Gangloff, R. Guillou, A. Deschamps, Nano-oxide precipitation kinetics during the consolidation process of a ferritic oxide dispersion strengthened steel, Scripta Materialia 188 (2020) 10–15, doi:10.1016/j.scriptamat.2020.07.003.

[61] A. Deschamps, F. de Geuser, Quantitative Characterization of Precipitate Microstructures in Metallic Alloys Using Small-Angle Scattering, Metallurgical and Materials Transactions A 44 (2013) 77–86, doi:10.1007/s11661-012-1435-7.

[62] P. Olier, M. Couvrat, C. Cayron, N. Lochet, L. Chaffron, Incidence of mechanical alloying contamination on oxides and carbides formation in ODS ferritic steels, Journal of Nuclear Materials 442 (2013) S106-S111, doi:10.1016/j.jnucmat.2013.03.090.

[63] A. Deschamps, F.D. Geuser, On the validity of simple precipitate size measurements by small-angle scattering in metallic systems, Journal of Applied Crystallography 44 (2011) 343–352, doi:10.1107/S0021889811003049.

[64] M. Dumont, L. Commin, I. Morfin, F. Degeuser, F. Legendre, P. Maugis, Chemical composition of nano-phases studied by anomalous small-angle X-ray scattering: Application to oxide nano-particles in ODS steels, Materials Characterization 87 (2014) 138–142, doi:10.1016/j.matchar.2013.11.008.

[65] M.H. Mathon, M. Perrut, S.Y. Zhong, Y. de Carlan, Small angle neutron scattering study of martensitic/ferritic ODS alloys, Journal of Nuclear Materials 428 (2012) 147–153, doi:10.1016/j.jnucmat.2011.12.010.

[66] C.P. Massey, S.N. Dryepondt, P.D. Edmondson, M.G. Frith, K.C. Littrell, A. Kini, B. Gault, K.A. Terrani, S.J. Zinkle, Multiscale investigations of nanoprecipitate nucleation, growth, and coarsening in annealed low-Cr oxide dispersion strengthened FeCrAl powder, Acta Materialia 166 (2019) 1–17, doi:10.1016/j.actamat.2018.11.062.

[67] A.J. Dianoux, G.H. Lander, Institut Laue-Langevin, Neutron data booklet, Old City, Philadelphia, PA, 2003 eds.2nd ed.

[68] I. Arganda-Carreras, V. Kaynig, C. Rueden, K.W. Eliceiri, J. Schindelin, A. Cardona, H.Sebastian Seung, Trainable Weka Segmentation: a machine learning tool for microscopy pixel classification, Bioinformatics 33 (2017) 2424–2426, doi:10.1093/bioinformatics/btx180.

[69] F.D. Geuser, W. Lefebvre, Determination of matrix composition based on solute-solute nearest-neighbor distances in atom probe tomography, Microscopy Research and Technique 74 (2011) 257–263, doi:10.1002/jemt.20899.

[70] S. Dhara, R.K.W. Marceau, K. Wood, T. Dorin, I.B. Timokhina, P.D. Hodgson, Atom probe tomography data analysis procedure for precipitate and cluster identification in a Ti-Mo steel, Data in Brief 18 (2018) 968-928. https://doi.org/doi.org/10.1016/j.dib.2018.03.094.

[71] H. Zhao, B. Gault, D. Ponge, D. Raabe, F. De Geuser, Parameter free quantitative analysis of atom probe data by correlation functions: Application to the precipitation in Al-Zn-Mg-Cu, Scripta Materialia 154 (2018) 106–110, doi:10.1016/j.scriptamat.2018.05.024.

[72] N. Sallez, P. Donnadieu, E. Courtois-Manara, D. Chassaing, C. Kübel, F. Delabrouille, M. Blat-Yrieix, Y. De Carlan, Y. Bréchet, On ball-milled ODS ferritic steel recrystallization: From as-milled powder particles to consolidated state, Journal of Materials Science 50 (2015) 2202–2217, doi:10.1007/s10853-014-8783-1.

[73] B.R. Pauw, C. Kästner, A.F. Thünemann, Nanoparticle size distribution quantification: results of a small-angle X-ray scattering inter-laboratory comparison, Journal of Applied Crystallography 50 (2017) 1280–1288, doi:10.1107/S160057671701010X.

[74] J.B. Seol, D. Haley, D.T. Hoelzer, J.H. Kim, Influences of interstitial and extrusion temperature on grain boundary segregation, Y−Ti−O nanofeatures, and mechanical properties of ferritic steels, Acta Materialia 153 (2018) 71–85, doi:10.1016/j.actamat.2018.04.046.

[75] Characterization of the nature and morphology of coarse precipitation in various oxide dispersion strengthened steels, Materialia 17 (2021) 101117, doi:10.1016/j.mtla.2021.101117.

[76] P. He, M. Klimenkov, R. Lindau, A. Möslang, Characterization of precipitates in nano structured 14% Cr ODS alloys for fusion application, Journal of Nuclear Materials 428 (2012) 131–138, doi:10.1016/j.jnucmat.2011.08.026.

[77] F. De Geuser, B. Gault, Metrology of small particles and solute clusters by atom probe tomography, Acta Materialia 188 (2020) 406–415, doi:10.1016/j.actamat.2020.02.023.

[78] E.A. Marquis, Core/shell structures of oxygen-rich nanofeatures in oxide-dispersion strengthened Fe-Cr alloys, Applied Physics Letters 93 (2008) 1–4, doi:10.1063/1.3000965.

[79] C.A. Williams, E.A. Marquis, A. Cerezo, G.D.W. Smith, Nanoscale characterisation of ODS-Eurofer 97 steel: An atom-probe tomography study, Journal of Nuclear Materials 400 (2010) 37–45, doi:10.1016/j.jnucmat.2010.02.007.

[80] Y. Dong, A. Etienne, A. Frolov, S. Fedotova, K. Fujii, K. Fukuya, C. Hatzoglou, E. Kuleshova, K. Lindgren, A. London, A. Lopez, S. Lozano-Perez, Y. Miyahara, Y. Nagai, K. Nishida, B. Radiguet, D.K. Schreiber, N. Soneda, M. Thuvander, T. Toyama, J. Wang, F. Sefta, P. Chou, E.A. Marquis, Atom Probe Tomography Interlaboratory Study on Clustering Analysis in Experimental Data Using the Maximum Separation Distance Approach, Microsc Microanal 25 (2019) 356–366, doi:10.1017/S1431927618015581.

[81] H. Sakasegawa, F. Legendre, L. Boulanger, M. Brocq, L. Chaffron, T. Cozzika, J. Malaplate, J. Henry, Y. De Carlan, Stability of non-stoichiometric clusters in the MA957 ODS ferrtic alloy, Journal of Nuclear Materials 417 (2011) 229–232, doi:10.1016/j.jnucmat.2010.12.056.

[82] R. Kasada, N. Toda, K. Yutani, H.S. Cho, H. Kishimoto, A. Kimura, Pre- and post-deformation microstructures of oxide dispersion strengthened ferritic steels, Journal of Nuclear Materials (2007) 222–228 367-370 A, doi:10.1016/j.jnucmat.2007.03.141.

[83] T. Liu, L. Wang, C. Wang, H. Shen, Effect of Al content on the oxidation behavior of Y2Ti2O7-dispersed Fe-14Cr ferritic alloys, Corrosion Science 104 (2016) 17–25, doi:10.1016/j.corsci.2015.11.025.

[84] S. Takaya, T. Furukawa, M. Inoue, T. Fujisawa, T. Okuda, F. Abe, S. Ohnuki, A. Kimura, Corrosion resistance of Al-alloying high Cr-ODS steels in stagnant lead-bismuth, Journal of Nuclear Materials 398 (2010) 132–138, doi:10.1016/j.jnucmat.2009.10.023.

[85] H. Dong, L. Yu, Y. Liu, C. Liu, H. Li, J. Wu, Effect of hafnium addition on the microstructure and tensile properties of aluminum added high-Cr ODS steels, Journal of Alloys and Compounds 702 (2017) 538–545, doi:10.1016/j.jallcom.2017.01.298.

[86] R. Ivanov, A. Deschamps, F. De Geuser, A combined characterization of clusters in naturally aged Al-Cu-(Li, Mg) alloys using small-angle neutron and X-ray scattering and atom probe tomography, Journal of Applied Crystallography 50 (2017) 1725–1734, doi:10.1107/S1600576717014443.

[87] L. Couturier, F. De Geuser, A. Deschamps, Direct comparison of Fe-Cr unmixing characterization by atom probe tomography and small angle scattering, Materials Characterization 121 (2016) 61–67, doi:10.1016/j.matchar.2016.09.028.

[88] M.K. Miller, C.M. Parish, Role of alloying elements in nanostructured ferritic steels, Materials Science and Technology 27 (2011) 729–734, doi:10.1179/1743284710Y.0000000039.

[89] M.S. Farkas, A.A. Bauer, The solid solubility and constitution of YTTRIUM in iron-20 TO 40 w/o Chromium Alloys, 1959. doi:10.2172/4206100.

[90] S.G. Epstein, A.A. Bauer, R.F. Dickerson, Solubility limits of yttrium and the lanthanide rare-earth elements in chromium and chromium-iron alloys, 1959. doi:10.2172/4194051.

[91] M.K. Miller, E.A. Kenik, K.F. Russell, L. Heatherly, D.T. Hoelzer, P.J. Maziasz, Atom probe tomography of nanoscale particles in ODS ferritic alloys, Materials Science and Engineering: A 353 (2003) 140–145, doi:10.1016/S0921-5093(02)00680-9.

[92] X. Boulnat, M. Perez, D. Fabrègue, S. Cazottes, Y. De Carlan, Characterization and modeling of oxides precipitation in ferritic steels during fast non-isothermal consolidation, Acta Materialia 107 (2016) 390–403, doi:10.1016/j.actamat.2016.01.034.